



HAL
open science

Ultraslow, slow, or fast spreading ridges: Arm wrestling between mantle convection and far-field tectonics

Laurent Husson, Philippe Yamato, Antoine Bézou

► To cite this version:

Laurent Husson, Philippe Yamato, Antoine Bézou. Ultraslow, slow, or fast spreading ridges: Arm wrestling between mantle convection and far-field tectonics. *Earth and Planetary Science Letters*, 2015, 429, pp.205-215. 10.1016/j.epsl.2015.07.052 . insu-01191512

HAL Id: insu-01191512

<https://insu.hal.science/insu-01191512>

Submitted on 2 Sep 2015

HAL is a multi-disciplinary open access archive for the deposit and dissemination of scientific research documents, whether they are published or not. The documents may come from teaching and research institutions in France or abroad, or from public or private research centers.

L'archive ouverte pluridisciplinaire **HAL**, est destinée au dépôt et à la diffusion de documents scientifiques de niveau recherche, publiés ou non, émanant des établissements d'enseignement et de recherche français ou étrangers, des laboratoires publics ou privés.

ridges reveal that the temperature variations are largest at shallow depths in the upper mantle, *i.e.* at the critical depth where the melt supply to the above ridges can be modulated, thereby also explaining why slow and ultraslow ridges are almost exclusively associated to cold mantle. It follows that the chemistry of oceanic ridge basalts may not strictly reveal the mantle potential temperature, but the variations in the sublithospheric temperature field.

9 *Key words:* ultraslow spreading ridges, mantle convection, plate tectonics, seismic tomography,
10 magmatism

11 1. Introduction

12 Mid-oceanic ridges display a wide range of tectonic velocities. Similarly to subduction rates, spreading
13 rates have been tentatively correlated to a variety of physical, geochemical, and morphological character-
14 istics of spreading ridges (e.g. Chen and Morgan, 1990; Bown and White, 1994; Shen and Forsyth, 1995;
15 Klein and Langmuir, 1987). The most striking results is the remarkably uniform crustal thickness for ridges
16 with spreading rate above 15 mm/yr (~ 7 km; Chen, 1992; White et al., 1992), excepted near hotspots and
17 fracture zones. However, this monotonic rule breaks down for very low spreading rates (*i.e.* at *ultraslow*
18 spreading ridges, below the threshold value of 15 mm/yr), where thinner crusts are systematically observed
19 (Reid and Jackson, 1981). The observation that the ultraslow South West Indian Ridge (*SWIR*) and Gakkel
20 ridges (fig. 1) are *a*-volcanic, and possibly *a*-magmatic (Cannat, 1993; Dick et al., 2003; Cannat et al., 2008),
21 eventually attests for a low melt supply that do not fulfills the demand for a ~ 7 km thick crustal layer. This
22 property has been interpreted as resulting from a variety of processes, including mantle composition (Zhou
23 and Dick, 2013), melt focussing within the mantle (Dick et al., 2003; Chen, 1992), along axis melt redistribu-
24 tion (Fox et al., 1995; Curewitz and Karson, 1998; Chen, 1992; Sauter et al., 2011), shortening of the melting
25 column within a thicker conductive thermal lid (Reid and Jackson, 1981), ridge obliquity relative to plate
26 motion (Dick et al., 2003), or simply by overall lower mantle temperature (Cannat, 1993). Hydrothermal
27 cooling within the variable fracture networks at slow and fast ridges is also often invoked (Phipps Morgan
28 and Chen, 1993). However, the cause of this lower thermal regime remains unclear at the ridge scale, for
29 departure from a mean spreading rate is also interpreted as depending on the deep thermal regime, implying
30 that buoyancy driven mantle flow controls the behavior of ridges (e.g. Sotin and Parmentier, 1989; Su et al.,
31 1994). Ultraslow ridges would correspond to a cool enough mantle to starve ridges from the magmatic supply.

32

*Corresponding author
Email addresses: laurent.husson@ujf-grenoble.fr (Laurent Husson)

33 Here, we explore the possibility that plate tectonics and continental drift not only modify plate velocities
34 -including spreading rates- but may also alter the pattern of the long-wavelength thermal regime of the
35 mantle, in particular at shallow depths where it may disturb oceanic accretion. We suggest that spreading
36 rates are not modulated by the vigor of the underlying mantle convection but instead by the tectonics acting
37 at the opposite plate boundaries. This reasoning is driven by kinematic clues: spreading of the *SWIR* was
38 twice faster before the Late Eocene onset of the Alpine collision between the African and Eurasian plates,
39 and gradually decreased from that time onwards (see for instance the reconstructions of Müller et al., 2008),
40 reflecting the declining northward absolute velocity of the African plate (e.g. Dewey et al., 1989; Silver
41 et al., 1998). To the North, the Alpine collision increased the resistance to plate motion and impedes further
42 northward motion of Africa; to the South, the Antarctic plate, being circumscribed by ridges, also opposes
43 any motion. Overall, we hypothesize that this change in the dynamics of the Tethyan margin modulated
44 the spreading rates of the *SWIR* down to its current value. The second modern example, *viz.* the Gakkel
45 ridge, always spread at low rates, due to the resistance at the opposed plate boundaries of the massive
46 Eurasian and North American continents that systematically precluded fast spreading. Overall, we suggest
47 that the effect of continental aggregation or slab anchoring at active margins is to prevent plate motion and
48 alter mantle flow by changing the surface boundary condition from mobile lid to sluggish or stagnant lid
49 (Yamato et al., 2013). This mechanism would in turn decrease the heat supply to the mantle underneath
50 ridges in particular, thereby modulating primordial features such as magmatic productivity and crustal
51 thickness, heat flow, ridge bathymetry, and lithospheric ageing. In the following, we investigate the intricate
52 relationships between plate tectonics, mantle convection and ridge spreading, first by means of an analysis
53 of the seismic geometry of the spreading lithospheres near their ridges, and secondly thanks to a thermo-
54 mechanical model designed to test our hypothesis on the dynamics of the system and to predict the thermal
55 evolution of the spreading lithosphere.

56 **2. Seismic structure of spreading lithospheres and mantle temperature variations**

57 The common understanding that the thermal structure of the lithosphere obeys a first-order dependence
58 on the square root of age has been inferred for long (e.g. Parsons and Sclater, 1977; Turcotte and Schubert,
59 2002). Seismic tomography independently validated this theory wherein oceanic plates are thermal boundary
60 layers cooling over the convecting mantle (Ritzwoller et al., 2004; Debayle and Ricard, 2012). But a closer
61 examination of the tomography model of Debayle and Ricard (2012) yields more: the age dependence of the
62 thermal structure of the lithosphere, which is satisfactorily evidenced when all plates are merged (fig. 2a),
63 improves when excluding slow moving lithospheres (<40 mm/yr, fig. 2b) and conversely degrades for slow
64 plates only (fig. 2c). Slow moving lithospheres are less well structured than faster ones. This threshold is
65 not random, as the analysis of Debayle and Ricard (2013) of the seismic anisotropy underneath the oceanic

66 lithospheres shows that only the motion of plates moving faster than 40 mm/yr correlates to mantle flow,
 67 while the direction of motion of slow (and ultraslow) plates does not. Although the observation could be
 68 biased because of the fact that the small motion of slow plates is more erratically assessed and can quickly
 69 depart from that of the global mantle flow, the interpretation that slow plates are less -if any- correlated to
 70 mantle flow statistically holds, regardless of the reference frame.

71
 72 This observation is even more striking when considering the spreading lithospheres in isolation, carefully
 73 selecting areas where ridges are spreading the most regularly (blue outlines in fig. 1). The seismic structure
 74 of the lithospheres degrades from fast, to slow, and ultraslow ridges (fig. 3): The *fastest spreading* East Pa-
 75 cific Rise and Pacific-Antarctic ridge display an unambiguous signature. To a lesser extent, the South-East
 76 Indian Ridge and the *slow spreading* lithospheres (South Atlantic, Central Indian, South Atlantic, Carls-
 77 berg, Central Atlantic and North Atlantic) still resemble a half-space cooling. Last, the *ultraslow* spreading
 78 lithospheres (SWIR and Gakkel) are completely unstructured. Following the analysis of seismic anisotropy
 79 of Debayle and Ricard, we interpret this degradation in the seismic signature as the fact that below a certain
 80 rate of spreading or absolute motion, plate tectonics are at odds with the underlying mantle circulation.
 81 At least, we interpret this observation as a symptom of a disturbed convective system for the mantle under
 82 slow spreading ridges.

83
 Another consideration arises from the fact that the oceanic lithospheres are thicker for slow spreading
 ridges (fig. 3). This implies that the parametrization for the half-space cooling theory needs to be adjusted
 depending on the spreading rate. When possible, we thus tentatively extract the thickness z of the thermal
 lithosphere from seismic tomography by assigning a specific wave speed anomaly to the bottom of the
 lithosphere (fig. 4a, for $\Delta V_s = 0\%$ and $\Delta V_s = -1\%$) at a common and supposedly mature age of 65-70
 Ma (to avoid local artifacts nearby ridges). The thickness of the seismic lithosphere clearly decreases with
 increasing spreading rates. One can further use this relationship as an indirect probe of the temperature
 variations in the sub-lithospheric mantle, on the basis of the half-space cooling theory, which relates the
 mantle temperature T_m to plate age t , such that

$$T_m = \frac{T_L - T_0}{\operatorname{erf}\left(\frac{z}{2\sqrt{\kappa t}}\right)} + T_0, \quad (1)$$

84 where T_0 is the surface temperature, T_L and z are the temperature and thickness of the thermal boundary
 85 layer, and κ is the thermal diffusivity (e.g. Turcotte and Schubert, 2002). Setting $T_0 = 0^\circ C$, $T_L = 1100^\circ C$
 86 and $\kappa = 1 \text{ mm s}^{-2}$ allows solving for T_m underneath each spreading ridge. Sublithospheric temperatures
 87 quickly drop -monotonously yet not linearly- with decreasing spreading rates.

88 Interpreting this temperature drop in terms of mantle temperature (reference value T_m^* , that would be
 89 the temperature underneath the *EPR* and Pacific-Antarctic) suggests that the mantle is $\sim 100^\circ C$ colder

90 beneath the *SEIR*, $\sim 100^\circ C$ beneath the *CIR* and South Atlantic ridges, $\sim 140^\circ C$ beneath the Carlsberg
91 ridge, and possibly $180^\circ C$ beneath the North Atlantic. The mantle under the Central Atlantic ridge is
92 also much colder than the fast-spreading ridges, but nevertheless slightly departs from the tendency. Of
93 course, this exercise has some limitations: first, it is only valid under the half-space cooling approximation,
94 which -based on the above observations- is increasingly erroneous with decreasing spreading rates; second,
95 ultraslow ridges are so unstructured (fig. 3) that any attempt to infer their lithospheric thicknesses -and
96 therefore the mantle temperatures that would derive from these estimates- is meaningless. Regardless, it
97 follows from the apparent relationship between spreading rates and sublithospheric mantle temperatures
98 that the mantle should be even colder underneath ultraslow spreading ridges. The slower oceanic plates
99 spread apart, the colder the underlying mantle temperature; by extrapolating the inferred relationship, we
100 thus anticipate that the mantle temperature underneath ultraslow spreading ridges is colder by $\sim 180^\circ C$
101 or more than the mantle temperature underneath fast spreading ridges, but only $\sim 50^\circ C$ than the mantle
102 temperature underneath slow spreading ridges.

103
104 Not surprisingly, the seismic signature of the mantle underneath the ridge also reveals the same ten-
105 dency. Although it would be particularly rash to directly convert wave speed anomalies into temperature
106 anomalies underneath ridges, we note that spreading rates globally correlate with wave speed anomalies
107 at sub-lithospheric depths, the faster the spreading the slower the shear wave velocity (figs. 3 and 4b).
108 This result is in accord with Humler et al. (1993) who found a correlation between basalt chemistry and
109 long wavelength pattern of seismic tomography underneath ridges. The more recent and therefore better
110 documented- tomography model that we use here confirms this trend at shorter wavelengths. Interestingly,
111 this correlation vanishes at depths and eventually becomes insignificant at depths greater than ~ 200 km,
112 suggesting that the thermal field is chiefly disturbed in the uppermost mantle. The sublithospheric mantle
113 temperature results from the competition between heat advection from below and heat conduction towards
114 the surface. Thus, our observation either suggests that conduction is higher or that advection is lower. The
115 following thermo-mechanical model allows to discriminate and rule out conduction as the sole possible cause.

116
117 Our investigation of the seismic tomography underneath the oceanic lithosphere outlines the links be-
118 tween spreading rates and mantle temperature. We also find that these relationships only hold down to
119 a critical value for spreading rates. Below this value (15 mm/yr, at the transition between the *slow* and
120 *ultraslow* spreading regimes) the half-space cooling model breaks down, suggesting that the mantle convects
121 regardless of the overriding spreading ridges, or at least in a partially incoherent manner. These findings
122 by themselves do not permit to discriminate an interpretation where a cool, feeble mantle flow is only able
123 to excite ridges at slow rates, from the alternative process that we explore below where it is plate tectonics
124 that modulates the upper kinematic condition for an equally vigorous mantle flow, and eventually alter the

125 general convective regime when spreading rates become too slow.

126

127 **3. Thermo-mechanical modeling of spreading ridges**

128 *3.1. A simplified model for the South West Indian Ridge, Tethyan subduction, and Alpine collision*

129 Our dynamic model is designed to capture the essential features of the *SWIR*, which is the most
130 documented of the poorly represented class of ultraslow ridges. Its spreading is likely controlled by a mantle
131 conveyor belt that drives the African plate from the *SWIR*, away from Antarctica and towards Eurasia.
132 More specifically, the African plate converges towards Eurasia, being pulled by the Tethyan subduction to
133 the North and pushed from the South (ridge push) and from below (mantle drag) by the upwelling mantle
134 arising from the African superplume (Lithgow-Bertelloni and Silver, 1998; Forte et al., 2010). A convection
135 cell, excited by the upwelling mantle to the South and the downwelling mantle to the North, propels the
136 African plate. But spreading rates decreased in the aftermath of the closure of the Tethys by more than 50%
137 (e.g. Müller et al., 2008). This temporal scenario therefore encompasses a variety of spreading settings, from
138 a *slow spreading* regime to an *ultraslow spreading* regime, that correspond to the pre- and post-collisional
139 times, respectively. Below we model the chain of consequences of the continental collision of the African
140 and Eurasian plates that opposes further divergence between the African and Antarctic plates, which in
141 turn altered the underlying mantle flow but not its power. This simplified model is designed to capture
142 the essential features of this scenario and predict the incidence of surface plate tectonics on mantle flow,
143 spreading rates, ridge geometry, mantle temperature and heat flow, that one can compare to independent
144 observables.

145 *3.2. Numerical model*

The numerical code used in this study is in two dimensions (2-D) and thermo-mechanically coupled. For details regarding its mechanical part, we refer to Yamato et al. (2012). It solves the Stokes equations (equations (2) and (3)) under the incompressibility constraint (4):

$$-\frac{\partial P}{\partial x} + \frac{\partial \sigma_{xx}}{\partial x} + \frac{\partial \sigma_{xz}}{\partial z} = 0, \quad (2)$$

$$-\frac{\partial P}{\partial z} + \frac{\partial \sigma_{zz}}{\partial z} + \frac{\partial \sigma_{zx}}{\partial x} = \rho g, \quad (3)$$

$$\frac{\partial V_x}{\partial x} + \frac{\partial V_z}{\partial z} = 0, \quad (4)$$

where P , σ_{ij} , ρ and g are the pressure, deviatoric stress tensor, density and gravitational acceleration, respectively. V_x and V_z are the two components of the velocity vector in the 2-D (x, z) Cartesian coordinate system. These equations are discretised on a Eulerian-staggered grid over the model domain using a finite

difference method (Gerya and Yuen, 2003, 2007). Material properties (viscosity and density) are carried by Lagrangian markers. At each time step, these properties are interpolated from the markers to the finite difference mesh using distance-dependent interpolation to solve the Stokes problem. All markers then move according to the obtained velocity field. This numerical scheme was already intensively tested (e.g. Yamato et al., 2012) and already applied with linear viscous materials at mantle convection scale (Yamato et al., 2013). For the thermal part, this code uses the formulation described and tested in Duprat-Oualid et al. (2013). The evolution of the temperature T through time t is obtained from the heat equation (5) expressed as:

$$\rho C_p \frac{\partial T}{\partial t} = \frac{\partial}{\partial x} \left(k \frac{\partial T}{\partial x} \right) + \frac{\partial}{\partial z} \left(k \frac{\partial T}{\partial z} \right) + Q, \quad (5)$$

where C_p , k and Q correspond to the heat capacity, thermal conductivity and heat production, respectively. This equation is discretized on the nodes of the Eulerian grid and solved using an implicit finite difference method. The computed temperature is then interpolated on markers and advected following the velocity field.

At each time step, the physical material properties as well as the temperature, defined on markers, move forward in time using a 4th order Runge-Kutta scheme. The thermal dependence of the viscosity and density is then applied to the markers. The viscosity is computed following Blankenbach et al. (1989), such as:

$$\eta = \eta_0 \cdot \exp \left(-\frac{b(T - T_0)}{\Delta T} + \frac{c(1 - z)}{h} \right), \quad (6)$$

where η_0 is the reference viscosity (at $T = T_0$, the surface temperature) and ΔT is the temperature difference between the bottom and the top of the model domain (see Table 1). The viscosity thus depends on temperature T and depth z , as defined in Blankenbach et al. (1989), b and c being constants (see Table 1) and h corresponding to the size of the model in the z -direction. We use the Boussinesq approximation and the density is computed as:

$$\rho = \rho_0 (1 - \alpha_v \cdot T), \quad (7)$$

146 where α_v corresponds to the thermal expansion coefficient (see Table 1). This thermo-mechanical code was
 147 satisfactorily tested on the benchmark cases 2(a) and 2(b) from Blankenbach et al. (1989). The numerical
 148 simulations presented in this study are, in a way, very similar to their benchmark case 2(b), excepted that
 149 the model size is different, that a lithosphere is added on top of the model and that a heat flux is imposed
 150 at the bottom right corner of the model box.

151

Our model is designed to mimic the evolution of the *SWIR*, yet in more generic sense. It is therefore simplified and two-dimensional (fig. 5). The mantle convects within a 10000 km wide and 3000 km deep

Cartesian box. The material is Newtonian and temperature and depth dependent, such that

$$\begin{aligned} \eta &= f(T, z), \text{ see eq.(6);} & \text{for } T > 1300^\circ C \\ \eta &= 10^{23} Pa s; & \text{for } T < 1300^\circ C \end{aligned}$$

152 The temperature threshold for $T < 1300^\circ C$ mimics the formation of the thermal boundary layer. In addi-
 153 tion, a continental lithosphere is represented by a 7500 km wide, 150 km thick neutrally buoyant unit (its
 154 density is that of the mantle) at high viscosity (set to $10^{25} Pa s$ to ensure minor strain) that rests atop the
 155 convecting mantle. The mechanical boundary conditions are free slip at all boundaries. Thermal boundary
 156 conditions impose a temperature drop ΔT of $3000^\circ C$ across the mantle thickness ($0^\circ C$ at the surface and
 157 $3000^\circ C$ at the core-mantle boundary), no lateral heat flow across the right and left side boundaries and a
 158 basal heat flow set to a uniform $100 mW m^{-2}$ excepted a the bottom right corner, where it is arbitrarily
 159 twice as high. This increased heat flow over 50 km on the bottom right is designed to polarize the convec-
 160 tive cell by focusing the upwellings below the spreading ridge, in accord with observations of ridges that
 161 are broadly located above active mantle upwellings (e.g. Alvarez, 1982; Husson et al., 2012). The thermal
 162 regime is dictated by a heat production at depth (away from the ridge) to avoid ridge-scale processes that
 163 are beyond our scope. The bulk production is set to compare to oceanic surface values (e.g. Pollack et al.,
 164 1993). Heat capacity Cp is set to $1250 J.kg^{-1}.K^{-1}$ in the whole model domain and conductivities are set
 165 to $5 W.m^{-1}.K^{-1}$ and $2.63 W.m^{-1}.K^{-1}$ for the mantle and the continental lithosphere, respectively. These
 166 values ensure that our model runs under standard conditions for the Rayleigh number $Ra_0 = 10^6$ and the
 167 Biot number $B = 10$ (e.g. Grigné et al., 2007).

168
 169 The initial rheological and density fields are dictated by the initial temperature field that is obtained
 170 after solving for the heat and Stokes equations in our model iteratively until a statistically convergent tem-
 171 perature field is achieved (after ~ 2 Ga). In order to do so, this precursor episode allows for free slip at the
 172 surface but artificially replaces the continent to its initial location throughout, at each time step. The initial
 173 temperature field in our model (fig. 5) is given by the time averaged temperature field over the last 500
 174 Myrs of this prior simulation. It allows for a statistically valid steady state thermal regime to be defined at
 175 all locations, including an upwelling underneath the *proto*-ridge (that corresponds to the thermal field just
 176 before continental breakup), an oceanic lithosphere on the left hand side of the continent that eventually
 177 subducts and forms a downwelling down to the core-mantle boundary, a thermal lid defined by the continent
 178 itself, drifting leftward under the action of the underlying mantle flow.

179
 180 This initial configuration therefore resembles the situation just prior to continental breakup, making the
 181 continent free to drift over its convection cell. It is pulled by a downwelling (to the left), pushed by an
 182 upwelling (to the right) and dragged by the flowing mantle (below). This setup permits to monitor the

183 evolution of the mantle temperature, viscosity and density fields during the journey of the continent over
184 its convection cell, until and after the collision with the left hand side boundary. As such, this scenario can
185 be regarded as a simplified model for the subduction of the Tethys, the Alpine collision and the African
186 superplume. On the right-hand side, it thus compares to the evolution of the *SWIR*, from the separation
187 between the Antarctic continent until the collision of Africa with Eurasia and thereafter, but also to any
188 ridge whose spreading tendency is impeded on the far-field (as for instance the South Atlantic, Silver et al.,
189 1998; Husson et al., 2012).

190 3.3. Results

191 The temporal evolution of our experiment is depicted by the stream function and viscosity field (fig.
192 6). The initial stage (until ~ 25 Myrs) correspond to the achievement of a statistical steady state of the
193 spreading regime and to the early development of the ridge, until half-spreading rates achieve ~ 125 mm/yr
194 (fig 7). During a second stage, the rates further increase, yet slowly, to almost 140 mm/yr at 100 Myrs
195 (model time). This increase results from the increasing pull of the subducting plate on the left hand side
196 (fig. 6). The model enters a third phase as the continent approaches the left boundary of the box. Because
197 of its positive buoyancy, the continent resists subduction and enters a collisional mode; because of its high
198 viscosity, strain rates are low; this gradually impedes further leftward migration of the continent, which
199 almost remains stationary throughout. The developing oceanic plate between the continent and the ridge
200 and the underlying mantle drag also undergoes compression but neither deforms for it is also highly viscous.
201 Under these conditions, spreading rates quickly collapse to very low values until ~ 175 Myrs. The model
202 then enters its last phase, where half-spreading rates are on the order of 1 mm/yr (note that this rate scales
203 with the viscosity and thicknesses of the oceanic and continental plates and could be adjusted accordingly).
204 This values keeps decreasing with time until the end of the model (fig. 7) as the oceanic plate cools and
205 thickens (fig. 6), thereby offering a growing resistance to the mantle driven compression.

206
207 The evolving motion of the plates exert an impact on the underlying mantle flow. Fundamentally, it
208 completely changes the upper kinematic boundary condition from a mobile lid convection regime to an
209 almost stagnant lid regime. During the transition between the two, the underlying mantle circulation is
210 entirely remodeled. While the early stages are characterized by a well defined, single convection cell (fig.
211 6a-c), the flow is disrupted during the final stages by the collision of the continent on the left hand side of
212 the model, and multiple cells arise (fig. 6c-e). Importantly, these cells are transient, and their short-lasting
213 nature is partially controlled by a growing number of thermally buoyant plumes. This reorganization has a
214 significant impact on mantle stirring and heat advection underneath the ridge, for the most proximal con-
215 vective cell to the spreading ridge alternates periods of vigorous upwelling driven by actively rising mantle
216 plumes (as at 200 Myrs, fig. 6d) and periods of relative quiescence during which the mantle underneath the

217 ridge is virtually ignored by the convective field (as at 250 Myrs, fig. 6e). On average during this period,
218 the sub-lithospheric mantle below the ridge is less vigorously stirred than during the pre-collisional stage
219 (see full length movie of the stream function online).

220
221 The thermal structure of both the mantle and the lithosphere is seriously impacted on the long-term.
222 During the pre-collisional stage (25-100 Myrs), the oceanic lithosphere that forms on the right hand side of
223 the model evolves according to the half-space cooling model (fig. 8a). It gently grows and the heat flow at
224 the ridge decreases down to a nearly stationary value of $\sim 100 \text{ mW}^{-2}$ at $\sim 75 \text{ Myrs}$ (fig. 7). (Note that
225 our simplified setup is not designed to comprehensively reproduce the thermal structure of the ridge itself:
226 the flow and temperature fields are mostly dictated by a temperature dependent rheology, that doesn't
227 account for ridge-scale processes like melt extraction; this simplification explains the rather long period of
228 decreasing heat flow (0-75 Myrs) before steady state is reached at the local scale). Once collision initiates
229 (from 100 Myrs onwards), spreading rates decrease and the structure of the oceanic lithosphere gradually
230 departs from a that of a steady half-space cooling model (fig. 8b). First, because the flow partly deserts the
231 mantle wedge below the ridge, the post-collisional convective regime advects less heat underneath the ridge.
232 Consequently, the expanding oceanic plate overall thickens and cools down at a faster rate than during the
233 pre-collisional stage. Between 120 and 180 Myrs, the heat flow drops accordingly and settle to some 50%
234 of the pre-collisional heat flow (fig. 7). Second, local gravitational instabilities are excited by the increas-
235 ingly chaotic convective regime. The thermal structure of the oceanic lithosphere consequently degrades
236 and departs from that of the half-space cooling model (fig. 8 and supplementary online material). The
237 gravitational instabilities that increasingly alter the structure of the lithosphere in the post-collisional phase
238 make its thickness vary in time and space, and the sub-lithospheric temperature be alternatively higher or
239 colder than if it were dictated by the half-space cooling model. This evolution -thickening of the lithospheric
240 lid and loss of its coherent structure- resembles the thermal structure inferred from seismic tomography (fig.
241 3); the variable spreading rates of the ridges at present-day thus represent different stages in the transition
242 scenario between mobile lid to stagnant lid.

243
244 The similarity between the model and observations from seismic tomography also holds for the vertical
245 temperature profile underneath the lithosphere: modeled temperature vary with the greatest amount at
246 shallow depths ($\sim 70\text{-}80 \text{ km}$, fig. 9), and wave speed heterogeneities are accordingly largest in the sub-
247 lithospheric mantle at similar depths (figs. 3 and 4b). This suggests that the temperature variations that
248 are induced by the changing boundary conditions are mostly located at shallow depths, *i.e.* at the most
249 appropriate depth to control the melt supply. The temperature field in the first 100 km prominently controls
250 the melting, and its evolution can be tracked by the depths of reference isotherms (1100° C and 1300° C ,
251 fig. 9a), that abruptly drop by 50% during the transient stage that follows the onset of collision, between

252 120 and 180 Myrs, before settling to ~ 50 km (1100° C) or ~ 60 km (1300° C). This cooling event of the
253 sublithospheric mantle is similarly depicted by the temperature at a constant depth underneath the ridge
254 (typically between 70 and 80 km, fig. 9b), that decrease by some 200° C. The thermal evolution of the
255 sublithospheric temperature is dictated by the competition between heat advection from the deeper mantle
256 and conduction towards the surface. Our models suggests that lower heat advection -and not a higher
257 conductivity- is responsible for a decrease in the potential temperature. Yet, our results do not rule out al-
258 ternative mechanisms, such as variable hydrothermal cooling (Phipps Morgan and Chen, 1993), but suggest
259 that a weakened heat advection from a slower convective regime that ignores the upper mantle is enough to
260 cool down slow spreading ridges at a fast rate.

261

262 4. Discussion

263 Our interpretation of the seismic tomography in terms of thermal structure of spreading lithosphere
264 suggest that it is the heat supply from the mantle, being modulated by plate tectonics, that permits -or not-
265 sufficient melting to grow a standard, 7 km thick, oceanic crust. Our thermal mechanical model confirms
266 this hypothesis, by showing that the upper kinematic conditions (mobile lid *vs.* stagnant lid) control the
267 convective regime of the mantle, and therefore the heat supply to the mantle that melts beneath the ridges.
268 More specifically, our model can be confronted to a variety of independent observables, that in turn allow
269 for a quantification of the process at play.

270

271 The melt productivity at oceanic ridges is key diagnostic of the mantle temperature underneath the ridge
272 (Klein and Langmuir, 1987; Shen and Forsyth, 1995), and corresponds to crustal thickness. The higher the
273 mantle temperature the more profuse partial melting is, and the thicker the crust. Our model suggests that
274 for a typical melting depth of 70-80 km, the temperature is lower by $\sim 200^\circ$ C in the stagnant lid (or post-
275 collisional) regime than in the mobile lid (pre-collisional) regime (fig. 9a). Along the same lines, the depth
276 of the isotherms 1100 - 1300° C increases by ~ 20 km, which further refrains the melting capacity (fig. 9b).
277 Such a weakening of the thermal regime, which corresponds to the entire range of inferred temperatures in
278 the samples of the present day mid-oceanic ridge system, is unambiguously sufficient to decrease the extent
279 of partial melting and starve the ridge from the magmatic supply -at least partially, if not entirely. As an ex-
280 ample, following the model of Klein and Langmuir (1987), we estimate that for such a temperature decrease,
281 the partial melt would drop from $\sim 13.5\%$ to less than $\sim 5\%$, which corresponds to a decrease in crustal
282 thickness from ~ 11 km to less than 2 km. Such a thin crustal thickness is comparable to the estimates
283 of partial melt and crustal thickness derived from the basalt chemistry or geophysical data collected in the
284 deepest sections of the SWIR and Gakkel ridges (Cannat, 1993; Jokat and Schmidt-Aursch, 2007; Michael

285 et al., 2003; Cannat et al., 2008; Standish et al., 2008). In addition, the surface heat flow at the ridge is also
286 diagnostic of the same process, and our model predictions suggest a decrease in heat flow by 40 mW m^{-2}
287 (fig. 7), compatible with the extrapolations of direct measurements (Pollack et al., 1993; Davies, 2013) that
288 possibly suggest that slow ridges are some 50 to 100% colder than fast spreading ridges, although ultraslow
289 ridges in particular are poorly documented.

290

291 In turn, it follows that the sublithospheric mantle field, modified by the evolving global convective pat-
292 tern, likely controls the chemistry of ridge basalts, which in turn could not strictly be used as a probe to
293 infer the deep mantle potential temperature.

294

295 Following our predictions, one should expect that partial melting was overall higher in the past and a
296 thicker crust associated with the fast spreading episode of the SWIR, before the onset of the African-Europe
297 collision in the late Eocene. This can in principle be tested from the chemical composition of ancient seafloor
298 basalts (as proposed by Humler et al., 1999; Fisk and Kelley, 2002; Brandl et al., 2013). Unfortunately avail-
299 able samples do not allow to generate high resolution transects orthogonally to the ridge to unravel such
300 temporal variations in mantle temperatures. Nonetheless, from a global perspective, the chemical composi-
301 tion of ancient seafloor basalts reveal anomalously hot mantle temperatures prior to 80 Ma (for the Atlantic
302 and Indian oceans, but not for the Pacific; Humler et al., 1999; Fisk and Kelley, 2002; Brandl et al., 2013).
303 Because continents act as thermal lids and raise their sub-lithospheric temperatures by $\sim 100^\circ\text{C}$ with re-
304 spect to the oceanic counterparts (Grigné and Labrosse, 2001; Lenardic et al., 2005; Coltice et al., 2007),
305 this observation was at first related to the effect of continental insulation (Humler and Besse, 2002). But the
306 case of the ultraslow Gakkel ridge, which remains cool regardless of its proximity to the continents (Humler
307 et al., 1999), jeopardizes this interpretation. Our model provides an alternative explanation that reconciles
308 these observations, as our results indicate that the mantle thermal heterogeneities sampled by mid-oceanic
309 ridges also responds efficiently to the feedback interaction between surface tectonics and mantle convection,
310 that may even overcome sub-continental heating.

311

312 Last, the model-predicted structure of the lithosphere is consistent with our observations of the global S-
313 wave seismic tomography model of Debayle and Ricard (2012): the transition from the mobile lid to stagnant
314 lid regime is accompanied by a decrease in the spreading rates and by a loss in the coherency of the thermal
315 structure of the lithosphere. Indeed, both the thermo-mechanical model (fig. 8) and the observations of the
316 seismic tomography (fig. 3) show that the geometry of freely spreading ridges satisfactorily reproduce the
317 half-space cooling model until spreading is blocked at the far field boundaries. Gravitational instabilities
318 then tend to develop and the lithospheric lid thickens underneath slow-spreading plates (fig. 6). The loss
319 in the structural coherency of the developing oceanic lithosphere and subsequent destabilization is partly

320 triggered by the increasing emergence of small scale, short lived thermal plumes during the post-collisional
321 stage. In our model, their number increases in the stagnant lid regime. In real Earth, oceanic plates are
322 riddled by plumes that accompany mantle upwellings (Boschi et al., 2007; Husson and Conrad, 2012). Their
323 surface expression in the abysses is however difficult to decipher, and seamounts may be considered as the
324 best available proxy for the distribution of submarine volcanism (see compilations by Kitchingman and
325 Lai, 2004; Hillier and Watts, 2007). If seamounts actually owe their existence to mantle plumes, one can
326 easily conclude from their apparent spatial distribution -only apparent because it is inferred from unevenly
327 spaced ship tracks- that mantle plumes are much more frequent in the vicinity of slow or ultraslow spreading
328 ridges than elsewhere (see Supplementary Information). This observation shall not be taken as a supporting
329 evidence of our model but instead as a highly compatible observation that further links our model to inde-
330 pendent features, and that may suggest that the mantle flow is more chaotic underneath slow- and ultraslow
331 spreading ridges.

332
333 Similarly, the fact that the mantle is more chaotic underneath slow spreading ridges is furthermore
334 documented by the chemistry of basalts, that is -conformably to crustal thickness- remarkably uniform for
335 spreading rates higher than 15 mm/yr, and much more heterogeneous for slower spreading rates (White
336 et al., 1992; Bown and White, 1994). The thermo-chemical regime underneath the mantle certainly controls
337 the melting and mixing processes (e.g. Klein and Langmuir, 1987). Yet, our model provides an alternative
338 explanation, as it suggests that the mantle underneath slow-spreading centers would be sampled from multi-
339 ple sources at different locations in the mantle (fig. 6), these sources possibly having different compositions.
340 Conversely, the stable pattern of mantle circulation underneath fast spreading ridges only allows for the
341 sampling of a unique reservoir in the upwelling mantle, preventing any heterogeneous signal. Note that this
342 observation doesn't imply that the mantle is less efficiently stirred underneath slow spreading ridges, or that
343 the temperature varies so as to generate incomplete melts, but instead that the chemical heterogeneity of
344 those ridges owes its existence to a more chaotic sampling of the mantle than elsewhere.

345 5. Conclusions

346 Current spreading rates vary from as much as 150 mm/yr in the fast East Pacific rise to almost null
347 values in some segments of the North Atlantic- Arctic system (Gakkel ridge), the entire range of velocities
348 being measured in between, and spreading rates have varied in the past (see the maps of Müller et al.,
349 2008). Based on our observations, reinforced by the results from our model, we suggest that these rates
350 are modulated by plate tectonics at the far field tectonics forces more than by the vigor of the underlying
351 mantle flow. The kinematics of ridges is driven by the competition between the global convective system
352 and crustal tectonics, as it is the case for subduction zones (Husson, 2012).

353

354

355

356

357

358

359

360

361

362

363

364

365

366

367

368

369

370

371

372

373

374

375

376

377

378

379

380

381

382

383

384

385

386

387

Our model depicts the genetic relationships between far-field tectonics and mantle flow during the transition from free continental drift to continental collision, and emphasizes that a unique mechanism build mountain belts in the far field, compresses the plates at the surface (Yamato et al., 2013), and controls the spreading rates of mid-oceanic ridges. The feedback interaction of the coupled system alters the dynamics of the system by changing the surface boundary condition, from a free slip regime toward a no slip regime. During this transition, the circulation of the mantle is drastically modified: while during the pre-collisional stage, it is characterized by a stationary single convection cell, the post-collisional stage features multiple convection cells that partially ignore the mantle wedge underneath the spreading ridges. The thermal incidence of this remodeled mantle dynamics is primordial, for it advects less heat underneath the ridge. The mantle there cools down, and consequently, lower amounts of partial melt are expected at ultraslow spreading ridges. Interestingly, both the model and the seismic structure of the mantle underneath ridges reveal that most of the variations in the thermal field are found at shallow depths, where it behaves as an extremely efficient control on the melt supply at ridges.

Our experiment therefore validates, or at least reveal the plausibility, of the hypothesized chain of relationships that we anticipated based on observations of the *SWIR* and Gakkel ridge. It is far-field tectonics that causes the starvation of basaltic melt underneath ultraslow spreading ridges. In the current model, collision is at play and alters the dynamics and thermal evolution of the mantle, but we emphasize that this model could be expanded to any ridge whose spreading tendency is restrained by far-field forces (as for instance the South Atlantic, Silver et al., 1998; Husson et al., 2012).

Finally, the joint analysis of the model and observations reveals that the regime of mantle convection drastically changes when the system is sufficiently blocked at the far ends to enter the stagnant lid regime, when ridges spread in the *ultraslow* regime, below 15 mm/yr (Reid and Jackson, 1981). We find that this threshold corresponds to the change in the magmatic supply of course, but also in the thermal structure of the lithosphere, as inferred from seismic tomography, heat flow, or ridge bathymetry, and clearly departs from the half-space cooling model below this threshold. These results support the idea that ultraslow ridges legitimately deserve the status of being a specific class of spreading ridges (Dick et al., 2003). Above that threshold, mantle flow doesn't seem to adjust to the rate of spreading, as the single-cell regime dominates. This conclusion is not drawn from our model but also from the observation that melting linearly adjust to spreading rates so as to grow a 7 km crust, suggesting that above a spreading rate of 15 mm/yr, the dynamic evolution of ridges is controlled by lithospheric processes more than deeper mantle convection. However, regardless of this first order distinction, other observations and model results indicate that slow and fast spreading ridges also belong to different classes: the thermal structure of slow ridges is less well structured,

388 their oceanic lithospheres are marked by a greater amount of seamounts, and short living plumes erode and
389 corrupt their thermal structures.

390

391 **Acknowledgements**

392 P.Y. thank P. Tackley and D. May for material support (ETH Brutus cluster). Comments from two
393 anonymous reviewers greatly improved the manuscript. Thanks to E. Debayle for sharing his model. Many
394 maps and plots were designed using the GMT (Generic Mapping Tools) software package (Wessel and Smith,
395 1991).

396 **References**

- 397 Alvarez, W., 1982. Geological evidence for the geographical pattern of mantle return flow and the driving mechanism of plate
398 tectonics. *Journal of Geophysical Research: Solid Earth* 87 (B8), 6697–6710.
399 URL <http://dx.doi.org/10.1029/JB087iB08p06697>
- 400 Blankenbach, B., Busse, F., Christensen, U., Cserepes, L., Gunkel, D., Hansen, U., Harder, H., Jarvis, G., Koch, M., Marquart,
401 G., Moore, D., Olson, P., Schmeling, H., Schnaubelt, T., Jul. 1989. A benchmark comparison for mantle convection codes.
402 *Geophysical Journal International* 98, 23–38.
- 403 Boschi, L., Becker, T. W., Steinberger, B., Oct. 2007. Mantle plumes: Dynamic models and seismic images. *Geochemistry,
404 Geophysics, Geosystems* 8, 10006.
- 405 Bown, J. W., White, R. S., Feb. 1994. Variation with spreading rate of oceanic crustal thickness and geochemistry. *Earth and
406 Planetary Science Letters* 121, 435–449.
- 407 Brandl, P. A., Regelous, M., Beier, C., Haase, K. M., May 2013. High mantle temperatures following rifting caused by
408 continental insulation. *Nature Geoscience* 6, 391–394.
- 409 Cannat, M., Mar. 1993. Emplacement of mantle rocks in the seafloor at mid-ocean ridges. *Journal of Geophysical Research* 98,
410 4163–4172.
- 411 Cannat, M., Sauter, D., Bezos, A., Meyzen, C., Humler, E., Le Rigoleur, M., Apr. 2008. Spreading rate, spreading obliquity,
412 and melt supply at the ultraslow spreading Southwest Indian Ridge. *Geochemistry, Geophysics, Geosystems* 9, 4002.
- 413 Chen, Y., Morgan, W. J., 1990. Rift valley/no rift valley transition at mid-ocean ridges. *Journal of Geophysical Research: Solid
414 Earth* 95 (B11), 17571–17581.
415 URL <http://dx.doi.org/10.1029/JB095iB11p17571>
- 416 Chen, Y. J., Apr. 1992. Oceanic crustal thickness versus spreading rate. *Geophysical Research Letters* 19, 753–756.
- 417 Coltice, N., Phillips, B. R., Bertrand, H., Ricard, Y., Rey, P., May 2007. Global warming of the mantle at the origin of flood
418 basalts over supercontinents. *Geology* 35, 391.
- 419 Curewitz, D., Karson, J. A., 1998. Geological consequences of dike intrusion at mid-ocean ridge spreading centers. Washington
420 DC American Geophysical Union Geophysical Monograph Series 106, 117–136.
- 421 Davies, J. H., Oct. 2013. Global map of solid Earth surface heat flow. *Geochemistry, Geophysics, Geosystems* 14, 4608–4622.
- 422 Debayle, E., Ricard, Y., Oct. 2012. A global shear velocity model of the upper mantle from fundamental and higher Rayleigh
423 mode measurements. *Journal of Geophysical Research (Solid Earth)* 117, 10308.
- 424 Debayle, E., Ricard, Y., Aug. 2013. Seismic observations of large-scale deformation at the bottom of fast-moving plates. *Earth
425 and Planetary Science Letters* 376, 165–177.

426 DeMets, C., Gordon, R. G., Argus, D. F., Stein, S., 1994. Effect of recent revisions to the geomagnetic reversal time scale on
427 estimates of current plate motions. *Geophysical Research Letters* 21, 2191–2194.

428 Dewey, J. F., Helman, M. L., Knott, S. D., Turco, E., Hutton, D. H. W., Jan. 1989. Kinematics of the western Mediterranean.
429 *Geological Society of London Special Publications* 45, 265–283.

430 Dick, H. J. B., Lin, J., Schouten, H., Nov. 2003. An ultraslow-spreading class of ocean ridge. *Nature* 426, 405–412.

431 Duprat-Oualid, S., Yamato, P., Pitra, P., Nov. 2013. Major role of shear heating in intracontinental inverted metamorphism:
432 Inference from a thermo-kinematic parametric study. *Tectonophysics* 608, 812–831.

433 Fisk, M., Kelley, K. A., Sep. 2002. Probing the Pacific’s oldest MORB glass: mantle chemistry and melting conditions during
434 the birth of the Pacific Plate. *Earth and Planetary Science Letters* 202, 741–752.

435 Forte, A. M., Quéré, S., Moucha, R., Simmons, N. A., Grand, S. P., Mitrovica, J. X., Rowley, D. B., Jul. 2010. Joint seismic-
436 geodynamic-mineral physical modelling of African geodynamics: A reconciliation of deep-mantle convection with surface
437 geophysical constraints. *Earth and Planetary Science Letters* 295, 329–341.

438 Fox, C. G., Radford, W. E., Dziak, R. P., Lau, T.-K., Matsumoto, H., Schreiner, A. E., Jan. 1995. Acoustic detection of a
439 seafloor spreading episode on the Juan de Fuca Ridge using military hydrophone arrays. *Geophysical Research Letters* 22,
440 131–134.

441 Gerya, T. V., Yuen, D. A., Jul. 2003. Rayleigh-Taylor instabilities from hydration and melting propel ‘cold plumes’ at subduction
442 zones. *Earth and Planetary Science Letters* 212, 47–62.

443 Gerya, T. V., Yuen, D. A., Aug. 2007. Robust characteristics method for modelling multiphase visco-elasto-plastic thermo-
444 mechanical problems. *Physics of the Earth and Planetary Interiors* 163, 83–105.

445 Grigné, C., Labrosse, S., 2001. Effects of continents on Earth cooling: Thermal blanketing and depletion in radioactive elements.
446 *Geophysical Research Letters* 28, 2707–2710.

447 Grigné, C., Labrosse, S., Tackley, P. J., Aug. 2007. Convection under a lid of finite conductivity: Heat flux scaling and
448 application to continents. *Journal of Geophysical Research (Solid Earth)* 112, 8402.

449 Hillier, J. K., Watts, A. B., Jul. 2007. Global distribution of seamounts from ship-track bathymetry data. *Geophysical Research*
450 *Letters* 34, 13304.

451 Humler, E., Besse, J., Oct. 2002. A correlation between mid-ocean-ridge basalt chemistry and distance to continents. *Nature*
452 419, 607–609.

453 Humler, E., Langmuir, C., Daux, V., 1999. Depth versus age: new perspectives from the chemical compositions of ancient
454 crust. *Earth and Planetary Science Letters* 173 (1–2), 7 – 23.
455 URL <http://www.sciencedirect.com/science/article/pii/S0012821X99002186>

456 Humler, E., Thiriot, J. L., Montagner, J. P., Jul. 1993. Global correlations of mid-ocean-ridge basalt chemistry with seismic
457 tomographic images. *Nature* 364, 225–228.

458 Husson, L., Dec. 2012. Trench migration and upper plate strain over a convecting mantle. *Physics of the Earth and Planetary*
459 *Interiors* 212, 32–43.

460 Husson, L., Conrad, C. P., Sep. 2012. On the location of hotspots in the framework of mantle convection. *Geophysical Research*
461 *Letters* 39, 17304.

462 Husson, L., Conrad, C. P., Faccenna, C., Feb. 2012. Plate motions, Andean orogeny, and volcanism above the South Atlantic
463 convection cell. *Earth and Planetary Science Letters* 317, 126–135.

464 Jokat, W., Schmidt-Aursch, M. C., Mar. 2007. Geophysical characteristics of the ultraslow spreading Gakkel Ridge, Arctic
465 Ocean. *Geophysical Journal International* 168, 983–998.

466 Kitchingman, A., Lai, S., 2004. Inferences on potential seamount locations from mid-resolution bathymetric data. *Fisheries*
467 *Centre Research Reports* 12 (5), 7–12.

468 Klein, E. M., Langmuir, C. H., Jul. 1987. Global correlations of ocean ridge basalt chemistry with axial depth and crustal

469 thickness. *Journal of Geophysical Research* 92, 8089–8115.

470 Kreemer, C., Oct. 2009. Absolute plate motions constrained by shear wave splitting orientations with implications for hot spot
471 motions and mantle flow. *Journal of Geophysical Research (Solid Earth)* 114, 10405.

472 Lenardic, A., Moresi, L.-N., Jellinek, A. M., Manga, M., Jun. 2005. Continental insulation, mantle cooling, and the surface
473 area of oceans and continents [rapid communication]. *Earth and Planetary Science Letters* 234, 317–333.

474 Lithgow-Bertelloni, C., Silver, P. G., Sep. 1998. Dynamic topography, plate driving forces and the African superswell. *Nature*
475 395, 269–272.

476 Michael, P. J., Langmuir, C. H., Dick, H. J. B., Snow, J. E., Goldstein, S. L., Graham, D. W., Lehnert, K., Kurras, G., Jokat,
477 W., Mühe, R., Edmonds, H. N., Jun. 2003. Magmatic and amagmatic seafloor generation at the ultraslow-spreading Gakkel
478 ridge, Arctic Ocean. *Nature* 423, 956–961.

479 Müller, R. D., Sdrolias, M., Gaina, C., Roest, W. R., Apr. 2008. Age, spreading rates, and spreading asymmetry of the world's
480 ocean crust. *Geochemistry, Geophysics, Geosystems* 9, 4006.

481 Parsons, B., Sclater, J. G., Feb. 1977. An analysis of the variation of ocean floor bathymetry and heat flow with age. *Journal*
482 *of Geophysical Research* 82, 803–827.

483 Phipps Morgan, J., Chen, Y. J., Apr. 1993. The genesis of oceanic crust: Magma injection, hydrothermal circulation, and
484 crustal flow. *Journal of Geophysical Research* 98, 6283–6298.

485 Pollack, H. N., Hurter, S. J., Johnson, J. R., Aug. 1993. Heat flow from the earth's interior - Analysis of the global data set.
486 *Reviews of Geophysics* 31, 267–280.

487 Reid, I., Jackson, H. R., Jun. 1981. Oceanic spreading rate and crustal thickness. *Marine Geophysical Research* 5, 165–172.

488 Ritzwoller, M. H., Shapiro, N. M., Zhong, S.-J., Sep. 2004. Cooling history of the Pacific lithosphere. *Earth and Planetary*
489 *Science Letters* 226, 69–84.

490 Sauter, D., Sloan, H., Cannat, M., Goff, J., Patriat, P., Schaming, M., Roest, W. R., Oct. 2011. From slow to ultra-slow: How
491 does spreading rate affect seafloor roughness and crustal thickness? *Geology* 39, 911–914.

492 Shen, Y., Forsyth, D. W., Feb. 1995. Geochemical constraints on initial and final depths of melting beneath mid-ocean ridges.
493 *Journal of Geophysical Research* 100, 2211–2237.

494 Silver, P., Russo, R., Lithgow-Bertelloni, C., 1998. Coupling of south american and african plate motion and plate deformation.
495 *Science* 279, 60–63.

496 Sotin, C., Parmentier, E. M., Aug. 1989. Dynamical consequences of compositional and thermal density stratification beneath
497 spreading centers. *Geophysical Research Letters* 16, 835–838.

498 Standish, J. J., Dick, H. J. B., Michael, P. J., Melson, W. G., O'Hearn, T., May 2008. MORB generation beneath the
499 ultraslow spreading Southwest Indian Ridge (9-25°E): Major element chemistry and the importance of process versus source.
500 *Geochemistry, Geophysics, Geosystems* 9, 5004.

501 Su, W., Mutter, C. Z., Mutter, J. C., Buck, W. R., Feb. 1994. Some theoretical predictions on the relationships among spreading
502 rate, mantle temperature, and crustal thickness. *Journal of Geophysical Research* 99, 3215–3227.

503 Turcotte, D. L., Schubert, G., Apr. 2002. *Geodynamics - 2nd Edition*. Wiley.

504 Wessel, P., Smith, W. H. F., 1991. Free software helps map and display data. *EOS Transactions* 72, 441–446.

505 White, R. S., McKenzie, D., O'Nions, R. K., Dec. 1992. Oceanic crustal thickness from seismic measurements and rare earth
506 element inversions. *Journal of Geophysical Research* 97, 19683.

507 Yamato, P., Husson, L., Becker, T. W., Pedoja, K., Dec. 2013. Passive margins getting squeezed in the mantle convection vice.
508 *Tectonics* 32, 1559–1570.

509 Yamato, P., Tartèse, R., Duret, T., May, D. A., Mar. 2012. Numerical modelling of magma transport in dykes. *Tectonophysics*
510 526, 97–109.

511 Zhou, H., Dick, H. J. B., Feb. 2013. Thin crust as evidence for depleted mantle supporting the Marion Rise. *Nature* 494,

Symbol	Value	Unit
η_0	8.1e22	<i>Pa.s</i>
ρ_0	4000	<i>kg.m⁻³</i>
T_0	0	<i>°C</i>
ΔT	3000	<i>°C</i>
h	3000	<i>km</i>
b^*	$\log(16384)$	–
c^*	$\log(64)$	–
g	10	<i>m.s⁻²</i>
α_v	2.5e-5	<i>K⁻¹</i>

Table 1: Model parameters. *: from Blankenbach et al. (1989)

513 **Supplementary information**

514 The full lengths movies of the experiment are provided online, including the stream function and viscosity
515 field (Sstreamvisco.m4v), full temperature field (Stempfull.m4v), and (sub-)lithosphere temperature field
516 (Stemplith.m4v).

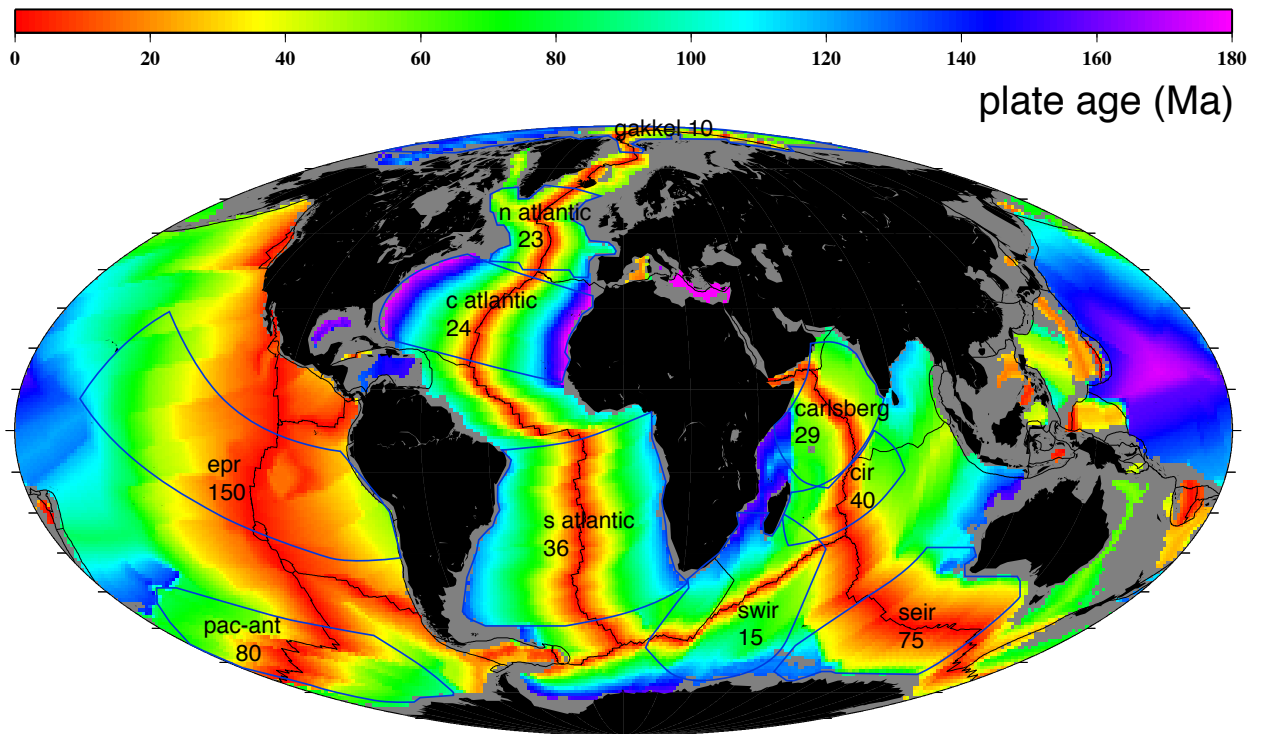


Figure 1: a) Seafloor age map (Müller et al., 2008). Ridge labels and maximum spreading rates (mm/yr). *epr*: East Pacific Rise (Nazca/Pacific); *pac – ant*: Pacific-Antarctic ridge (Pacific/Antarctic); *seir*: South East Indian Ridge (Australia/Antarctic); *s atlantic*: South Atlantic ridge (Africa/South America); *carlsberg*: Carlsberg ridge (Africa/India); *c atlantic*: Central Atlantic ridge (North America/Africa); *n atlantic*: North Atlantic ridge (Eurasia/North America); *swir*: South West Indian Ridge (Antarctic/Africa); *gakkel*: Gakkel ridge (Eurasia/North America). Blue contours delineate the location of the oceanic domains considered for oceanic plate pairs across ridges.

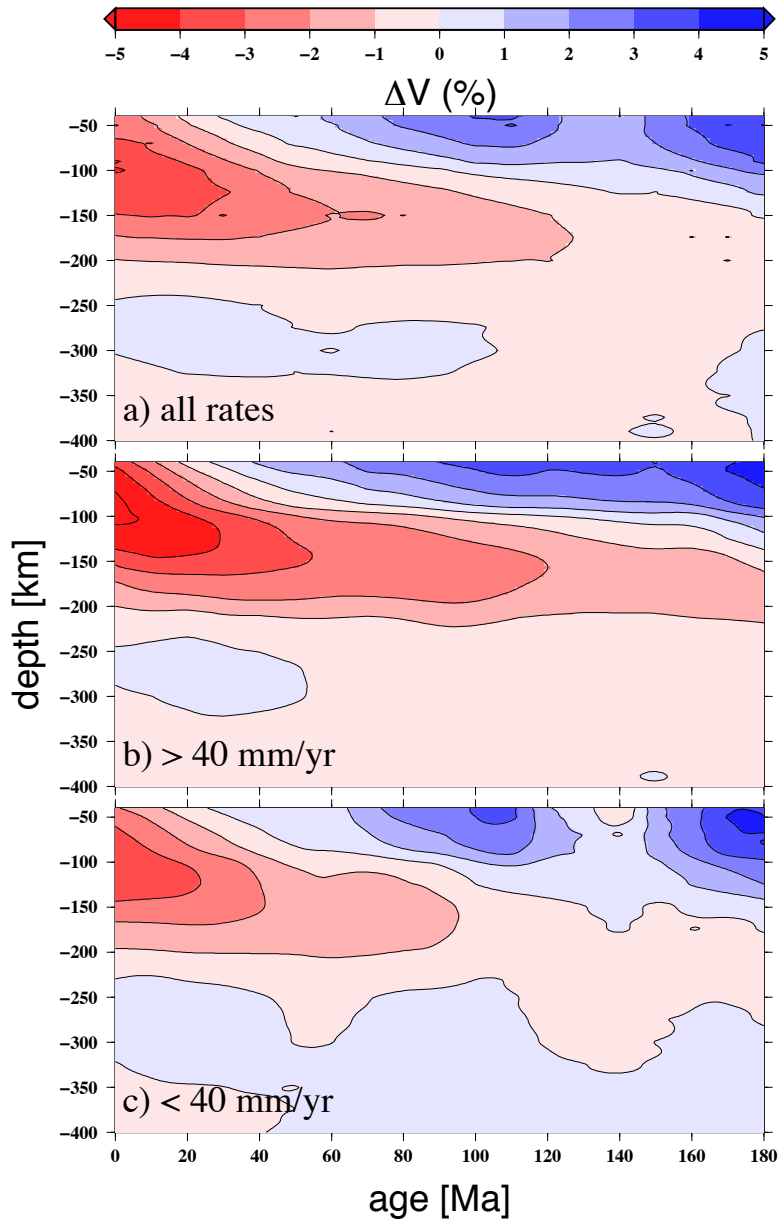


Figure 2: Synthetic cross-sections across the S wave tomographic model of Debayle and Ricard (2012) for all oceanic plates, sampled at all locations (a) and where the absolute motion is faster (b) and slower (c) than 40 mm/yr (plate motion from Kreemer, 2009). Color scale indicates the wave speed anomalies (in %) with respect to their reference model.

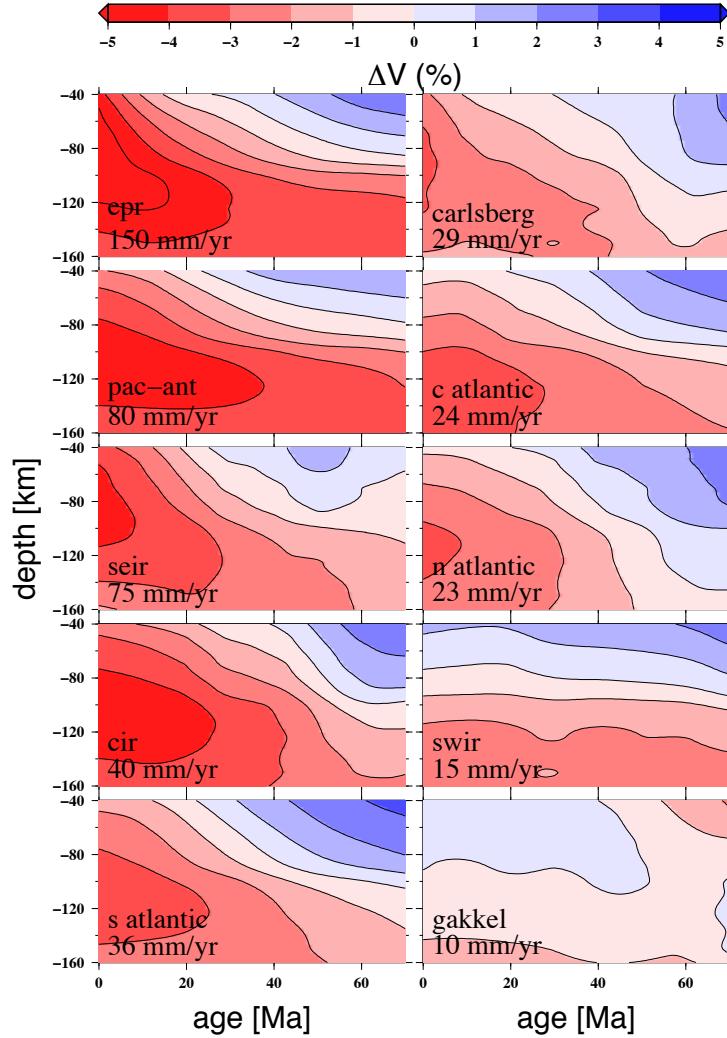


Figure 3: Synthetic cross-sections across the S wave tomographic model of Debayle and Ricard (2012) for oceanic plate pairs across ridges (see location fig. 1). *epr*: East Pacific Rise (Nazca/Pacific); *pac-ant*: Pacific-Antarctic ridge (Pacific/Antarctic); *seir*: South East Indian Ridge (Australia/Antarctic); *s atlantic*: South Atlantic ridge (Africa/South America); *carlsberg*: Carlsberg ridge (Africa/India); *c atlantic*: Central Atlantic ridge (North America/Africa); *n atlantic*: North Atlantic ridge (Eurasia/North America); *swir*: South West Indian Ridge (Antarctic/Africa); *gakkel*: Gakkel ridge (Eurasia/North America). Rates in mm/yr are full spreading rates.

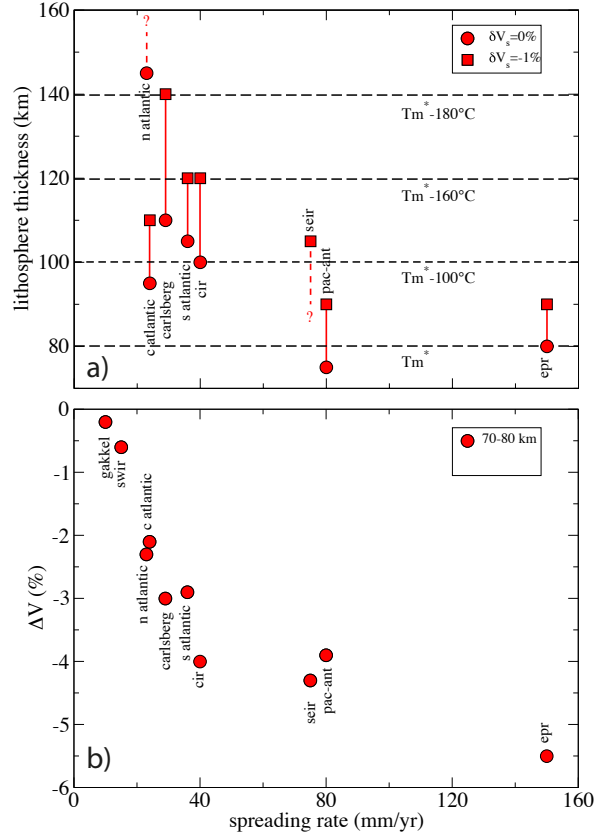


Figure 4: a) Depths of the wave speed anomalies $\delta V_s = 0\%$ (circles) and $\delta V_s = -1\%$ (squares) underneath spreading lithospheres at 65-70 Ma (inferred from the synthetic age-depth cross-sections of oceanic plates, derived from the S wave tomographic model of Debayle and Ricard, 2012, as a function of spreading rates (NUVEL1, DeMets et al., 1994), for individual spreading ridges (see fig. 3). These depths are taken as proxies for lithosphere thickness. Lithosphere thickness converts into mantle temperature, following a half-space cooling model (e.g. Parsons and Sclater, 1977; Turcotte and Schubert, 2002). Dashed lines are abaqus showing the mantle temperature with respect to the temperature T_m^* below a 80 km thick lithosphere. b) Magnitude of the wave speed anomalies δV_s underneath the ridge, as a function of spreading rate.

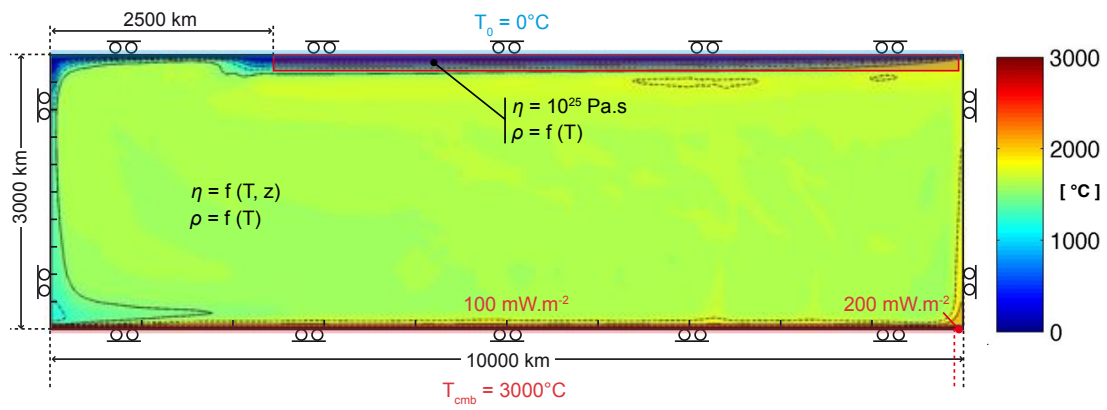


Figure 5: Model setup and initial temperature field. The red rectangle at the surface delineates the highly viscous continental lithosphere. T_0 and T_{CMB} are the temperatures at the surface and the core-mantle boundary. Rollers indicate free-slip boundary conditions. See text for all details regarding the numerical scheme and initial and boundary conditions.

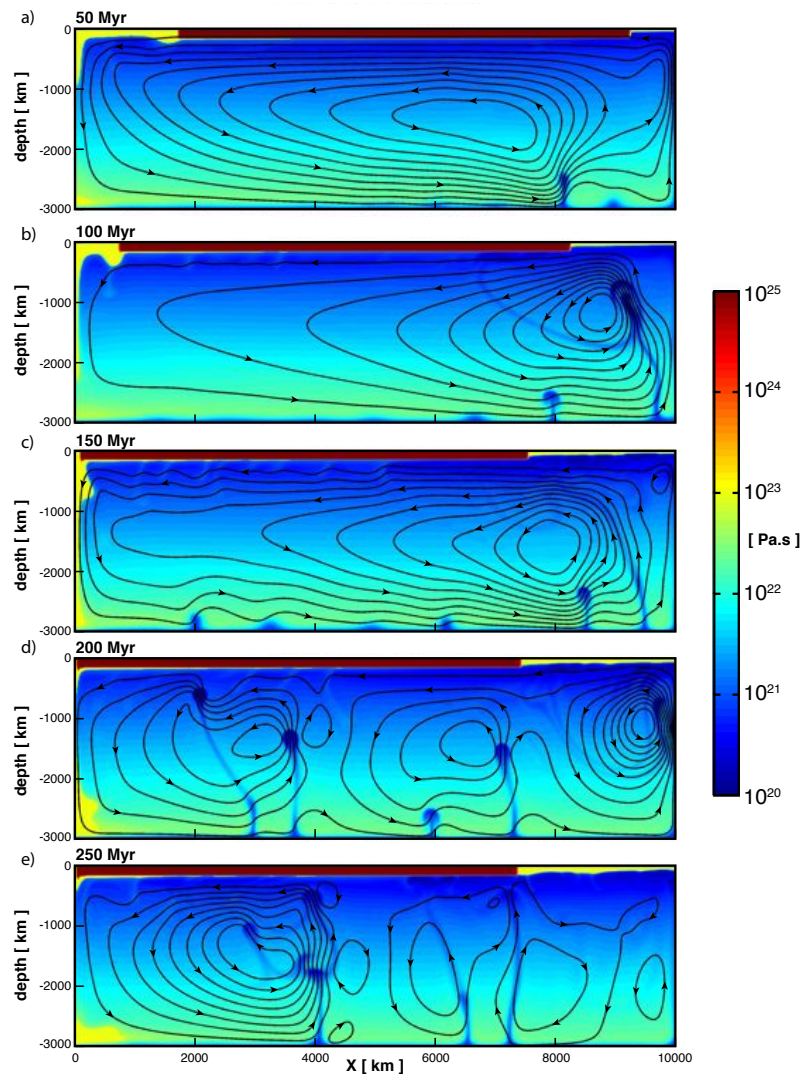


Figure 6: Stream function (curves) and viscosity field (colored background) sampled with a 50 Myrs time step. The transition from a mobile lid regime to a quasi stagnant lid regime occurs between 150 Myrs and 200 Myrs.

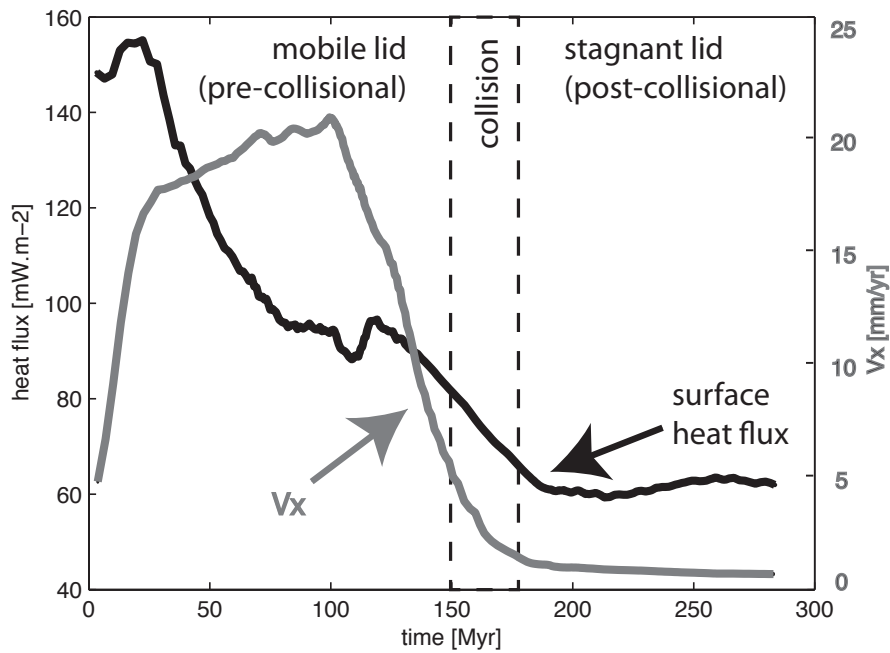


Figure 7: Modeled half-spreading rates V_x (horizontal velocity at the ridge), and heat flux at the ridge, as a function of time. Dashed lines outline the approximate timing of collision and the transition between the mobile lid and stagnant lid regimes of mantle convection.

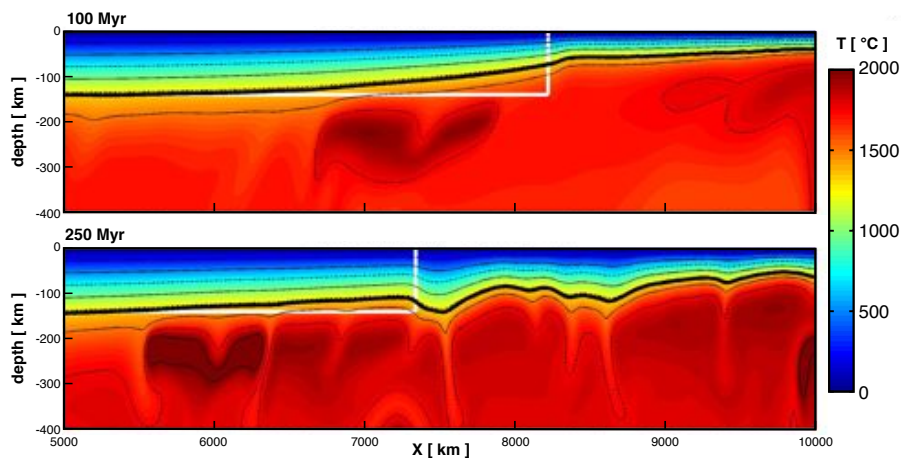


Figure 8: Temperature field in the upper mantle and lithosphere at 100 Ma (pre-collisional stage, top) and 250 Ma (post-collisional stage, bottom). White box delineates the continental lithosphere.

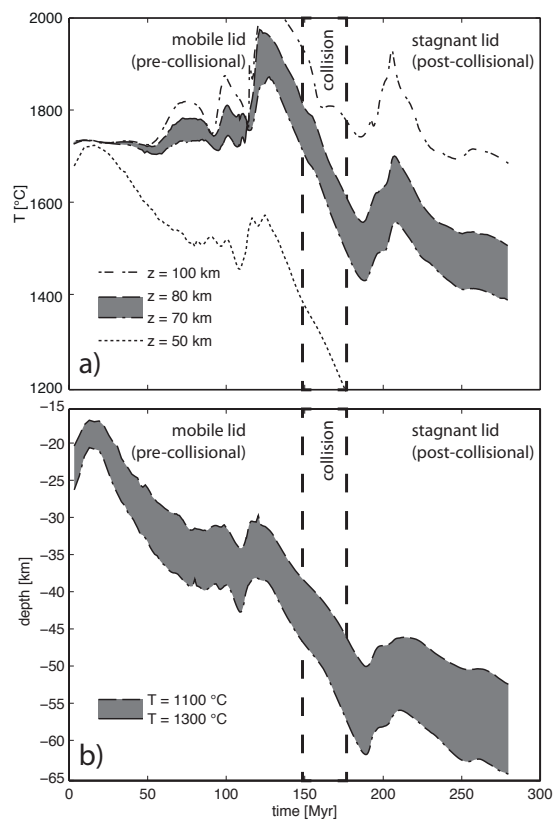
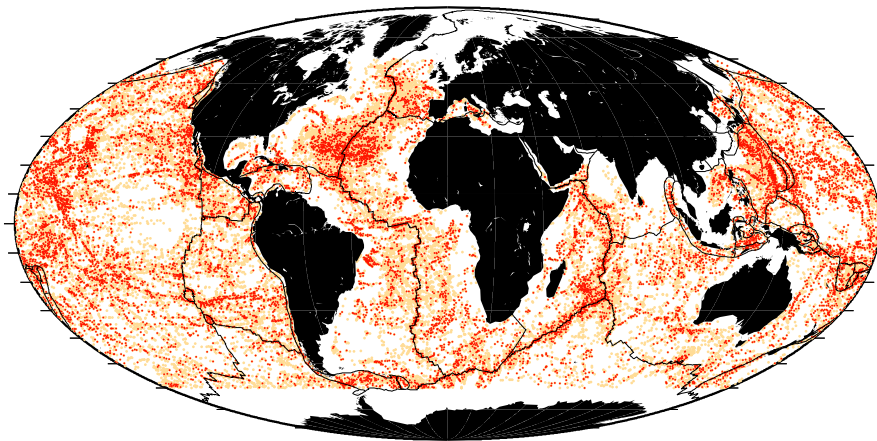


Figure 9: a) Temperature at 50 km (dotted), between 70 and 80 km depth (gray) and at 100 km (dot-dashed) as a function of time. b) Isothermal depth (between 1100° and 1300°) underneath the ridge.



Supplementary figure: location of seamounts higher than 500 m (orange dots) and 1000 m (red dots). Fast spreading ridges (EPR, Pac-Ant, and SEIR) are seemingly deprived of seamounts with respect to slow-spreading (for example North and Central Atlantic, CIR) and ultraslow spreading ridges (SWIR).

Figure1

[Click here to download Figure: f1_map.pdf](#)

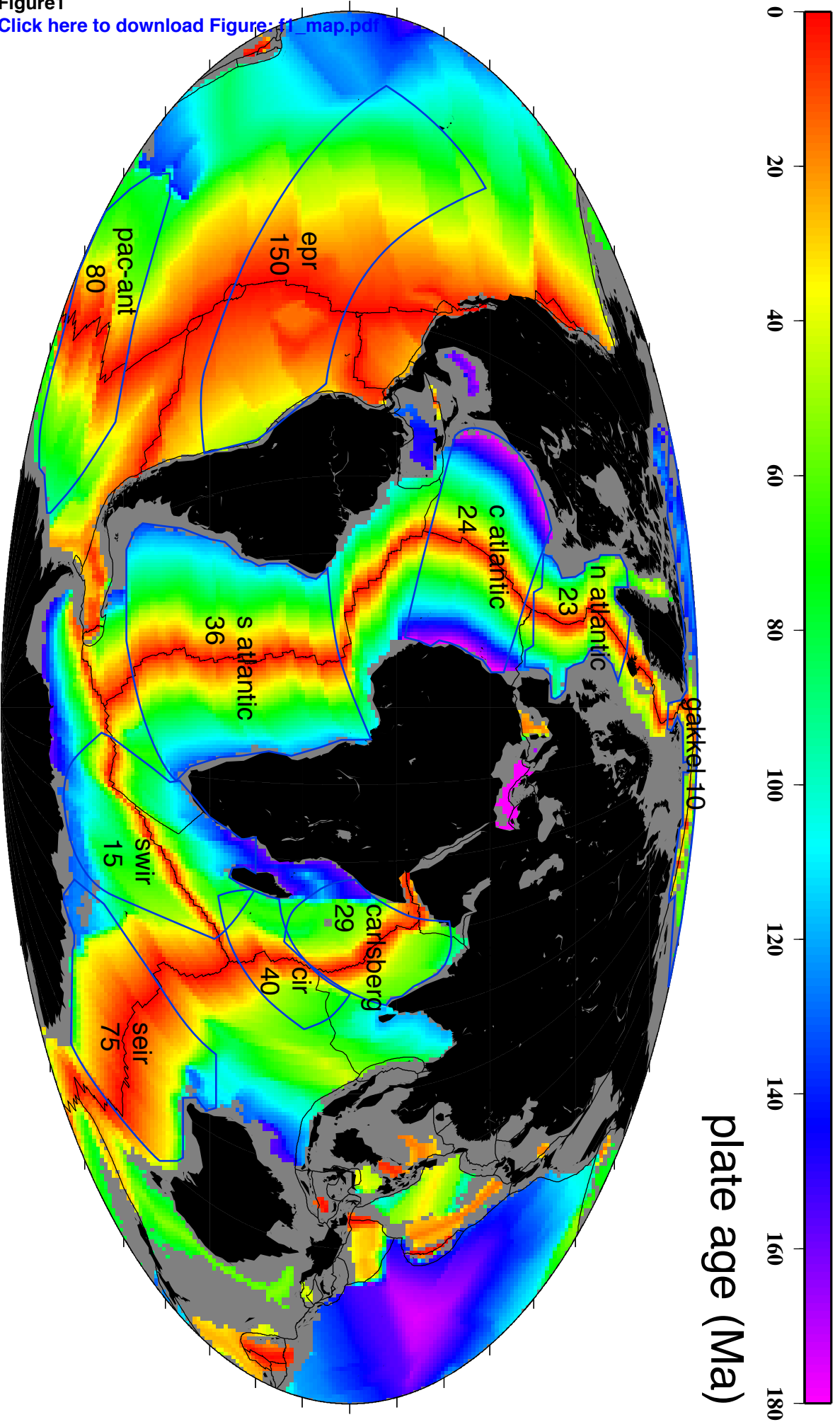


Figure2

[Click here to download Figure: f2_tomov40.pdf](#)

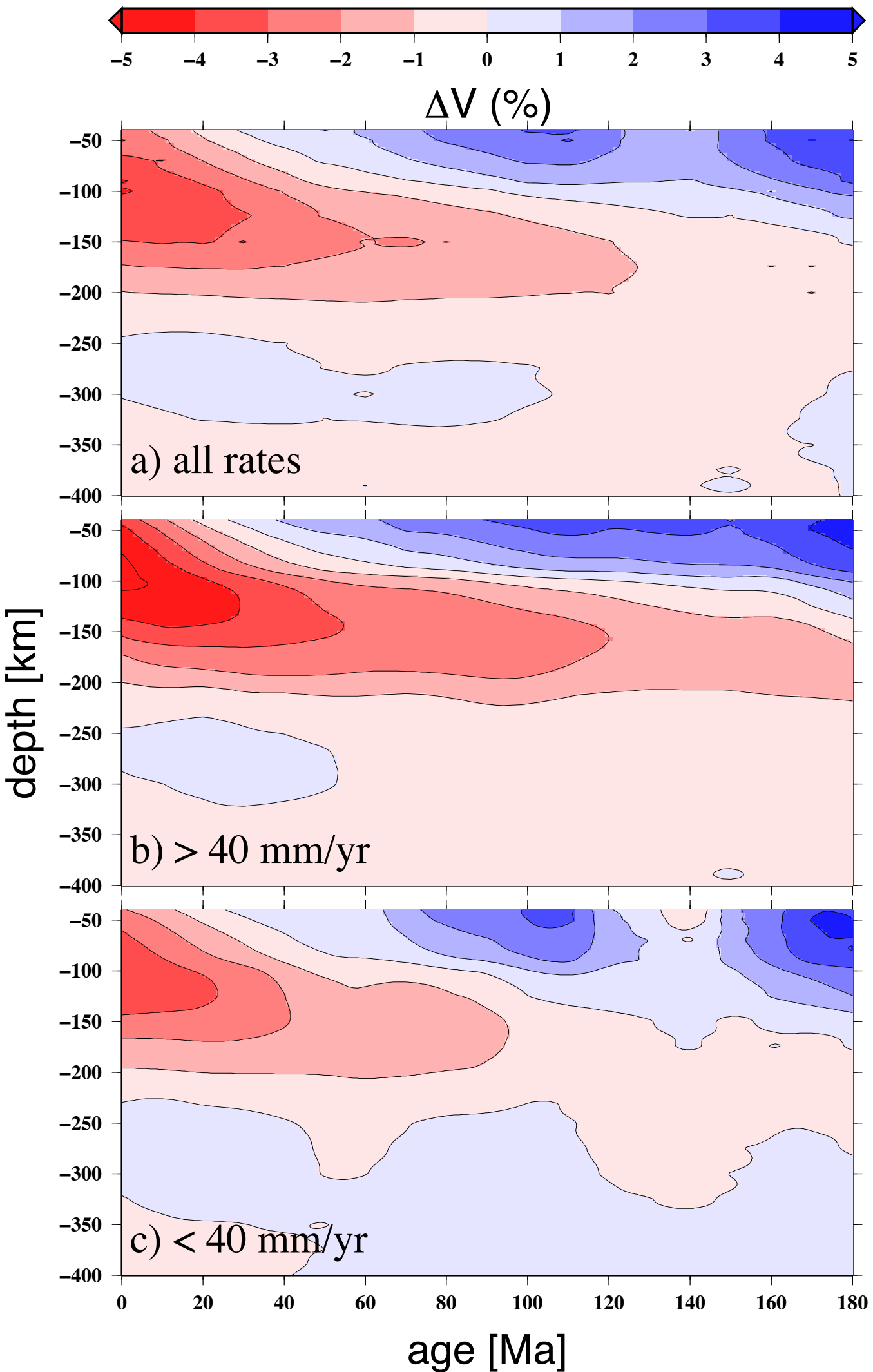


Figure3

[Click here to download Figure: f3_tomoplate.pdf](#)

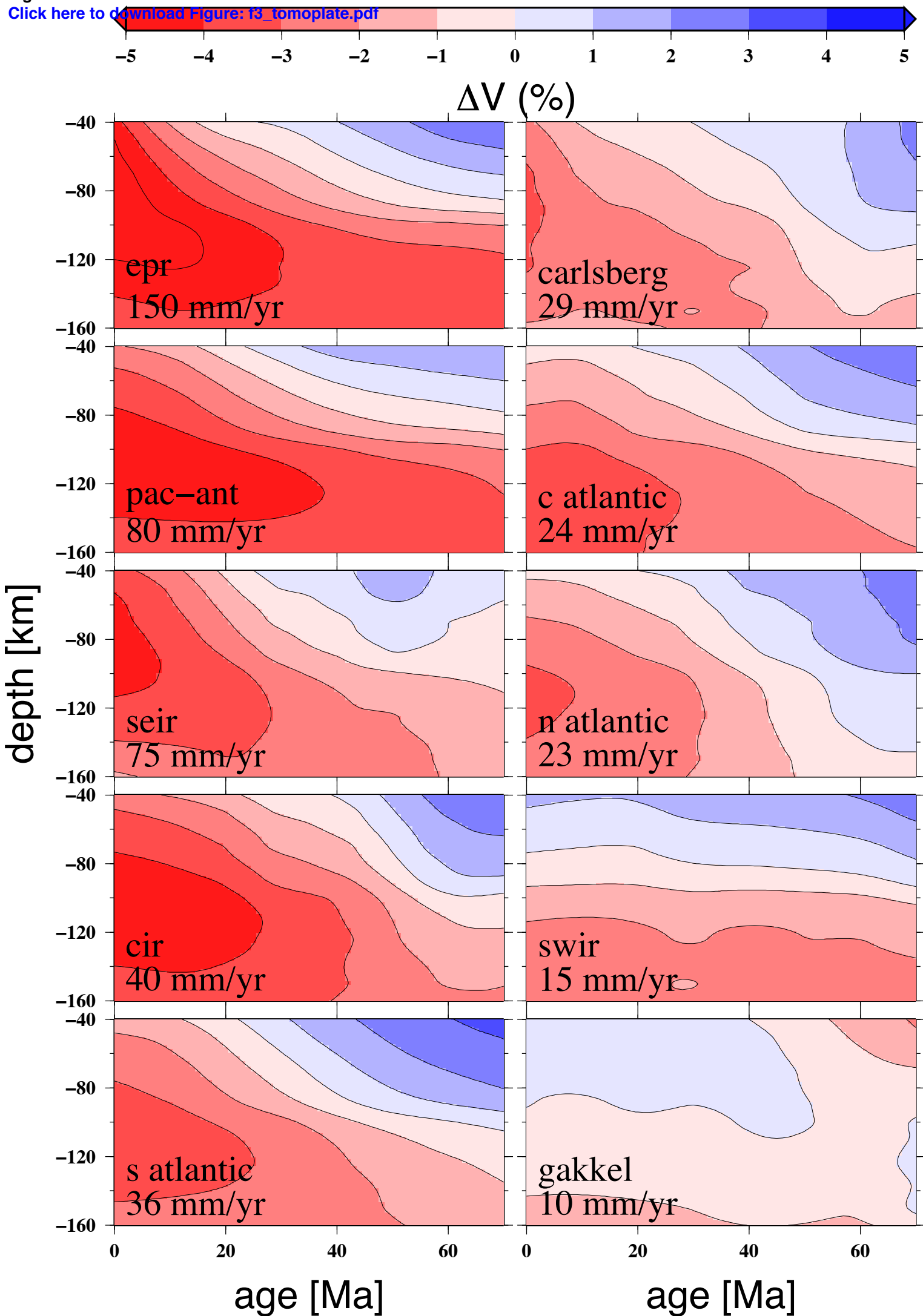


Figure4
[Click here to download Figure: f4_flat1.pdf](#)

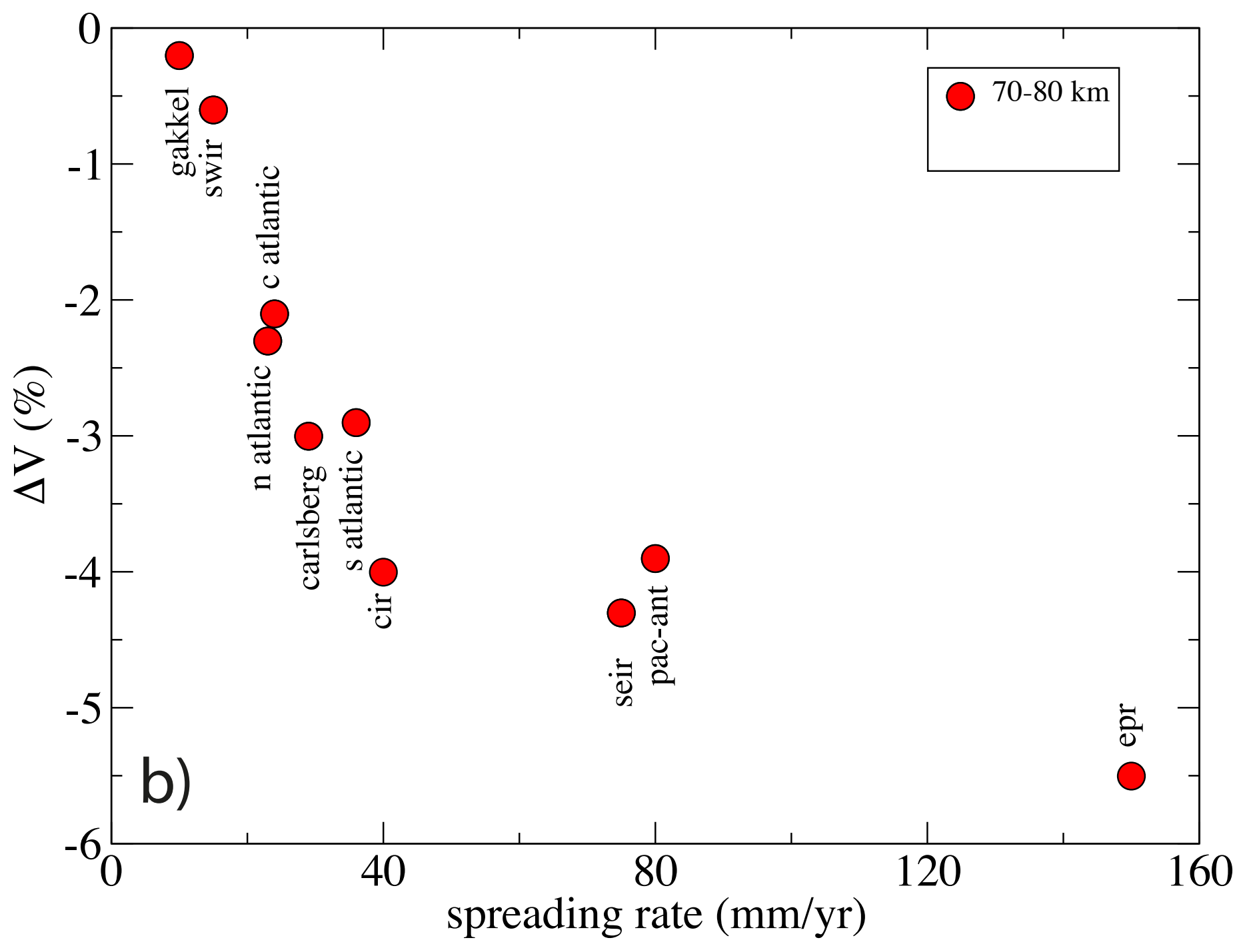
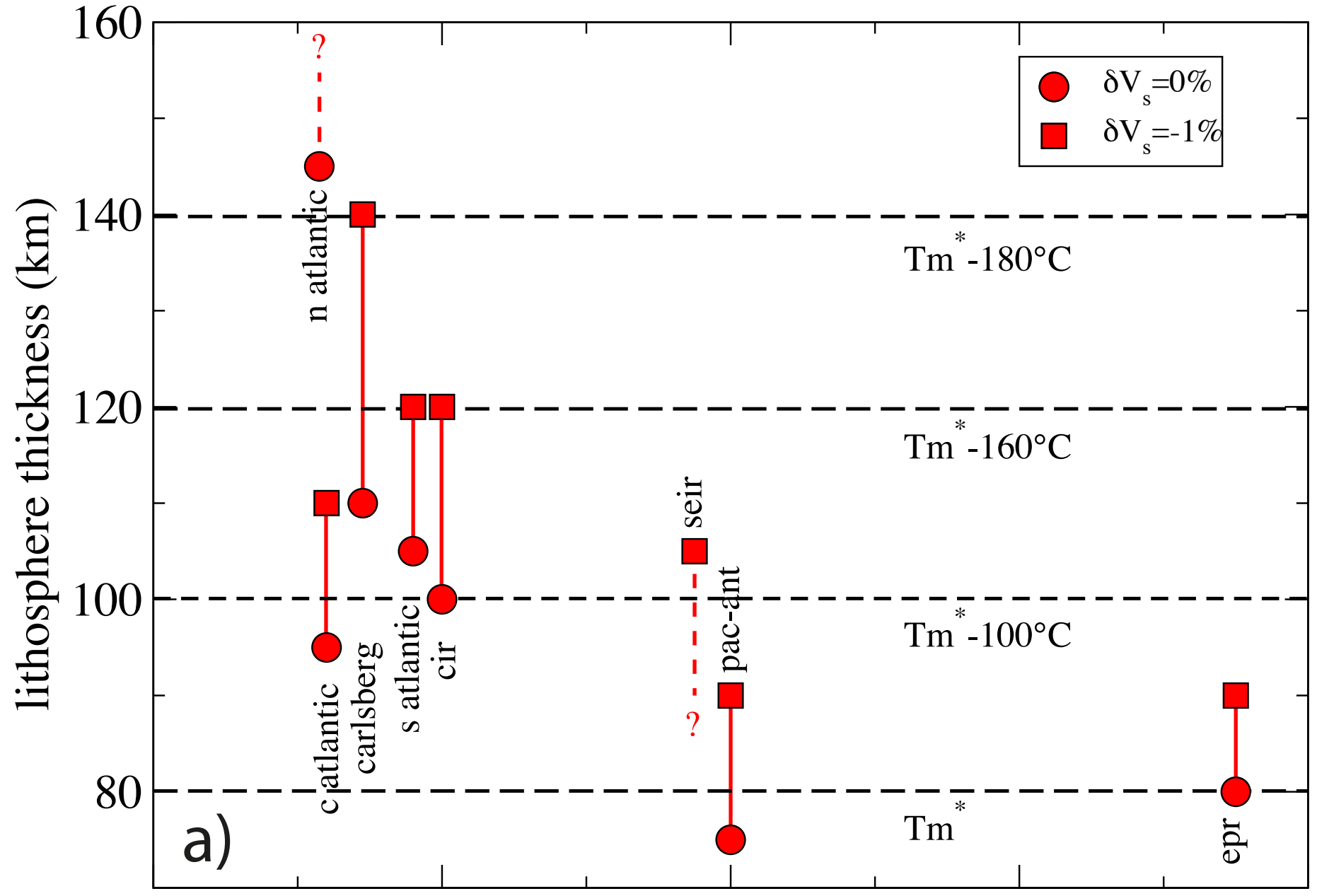


Figure 5

[Click here to download Figure: f5_initLR.pdf](#)

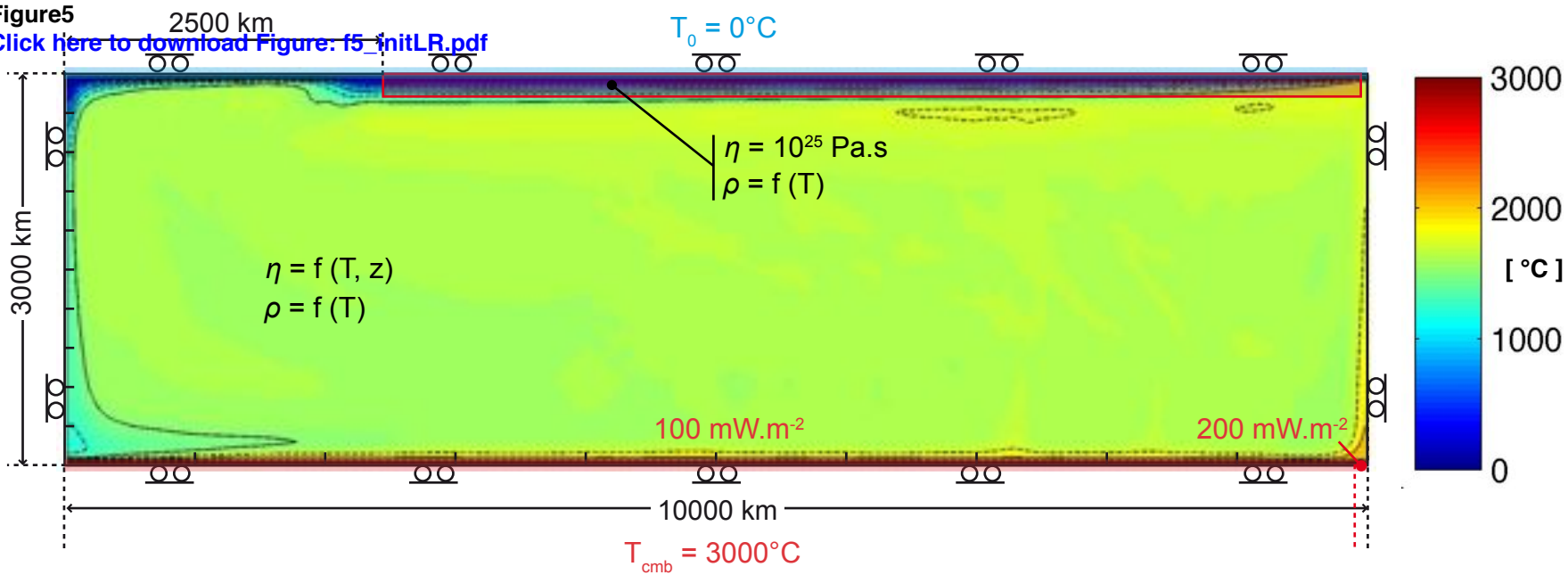
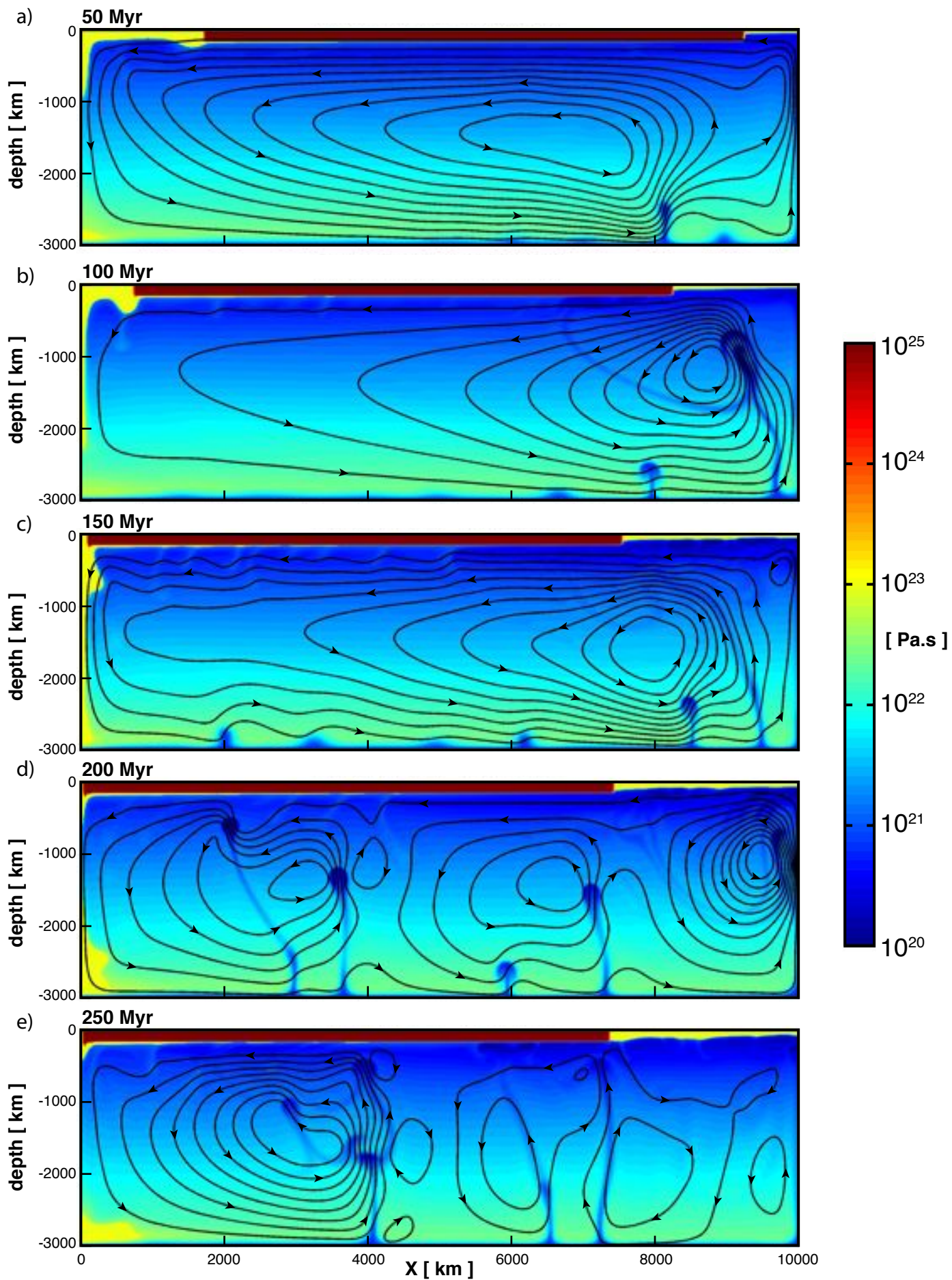


Figure6

[Click here to download Figure: f6_streamLR.pdf](#)



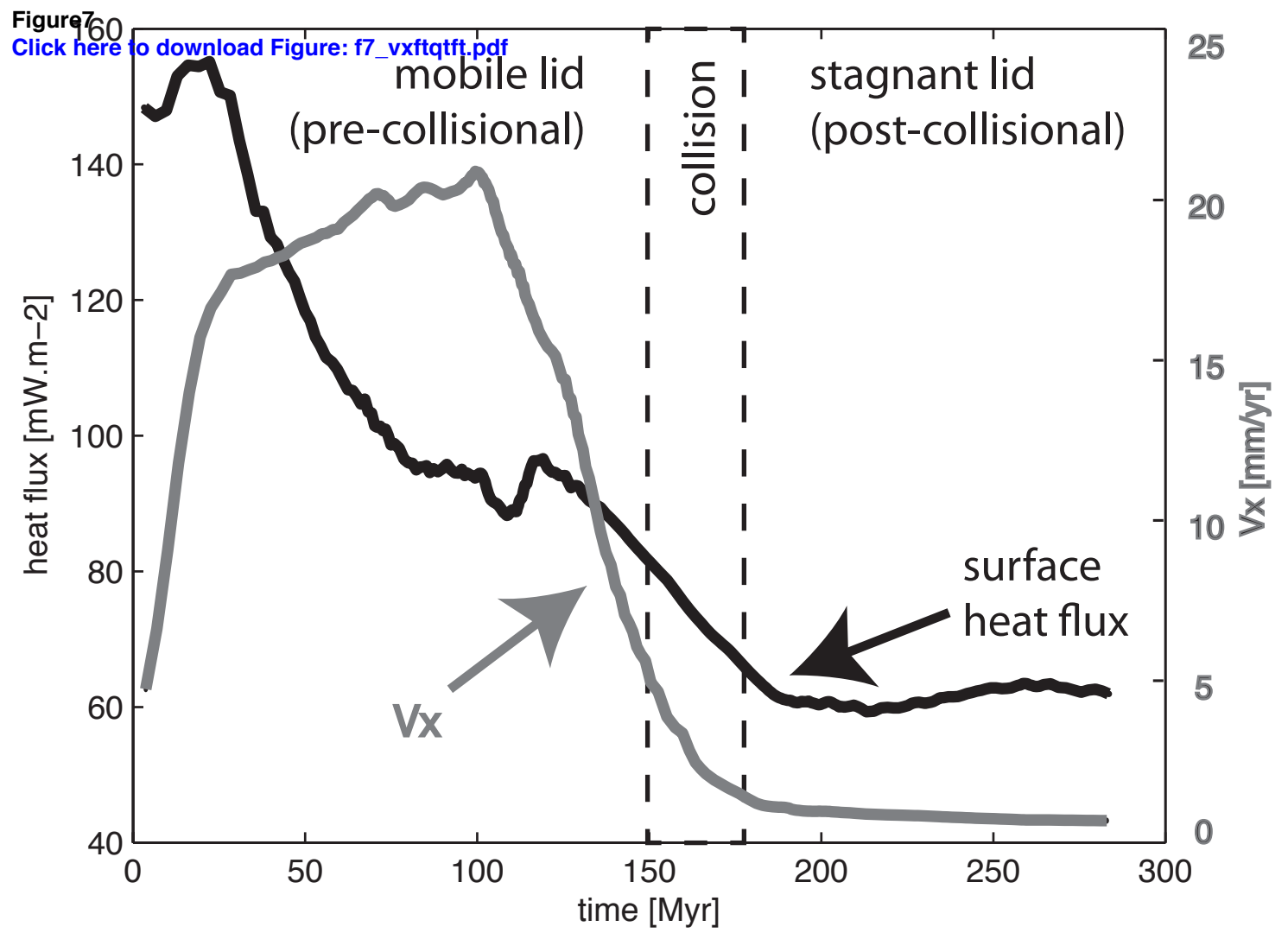


Figure 8 100 Myr

[Click here to download Figure: f8_Tzoom1.R.pdf](#)

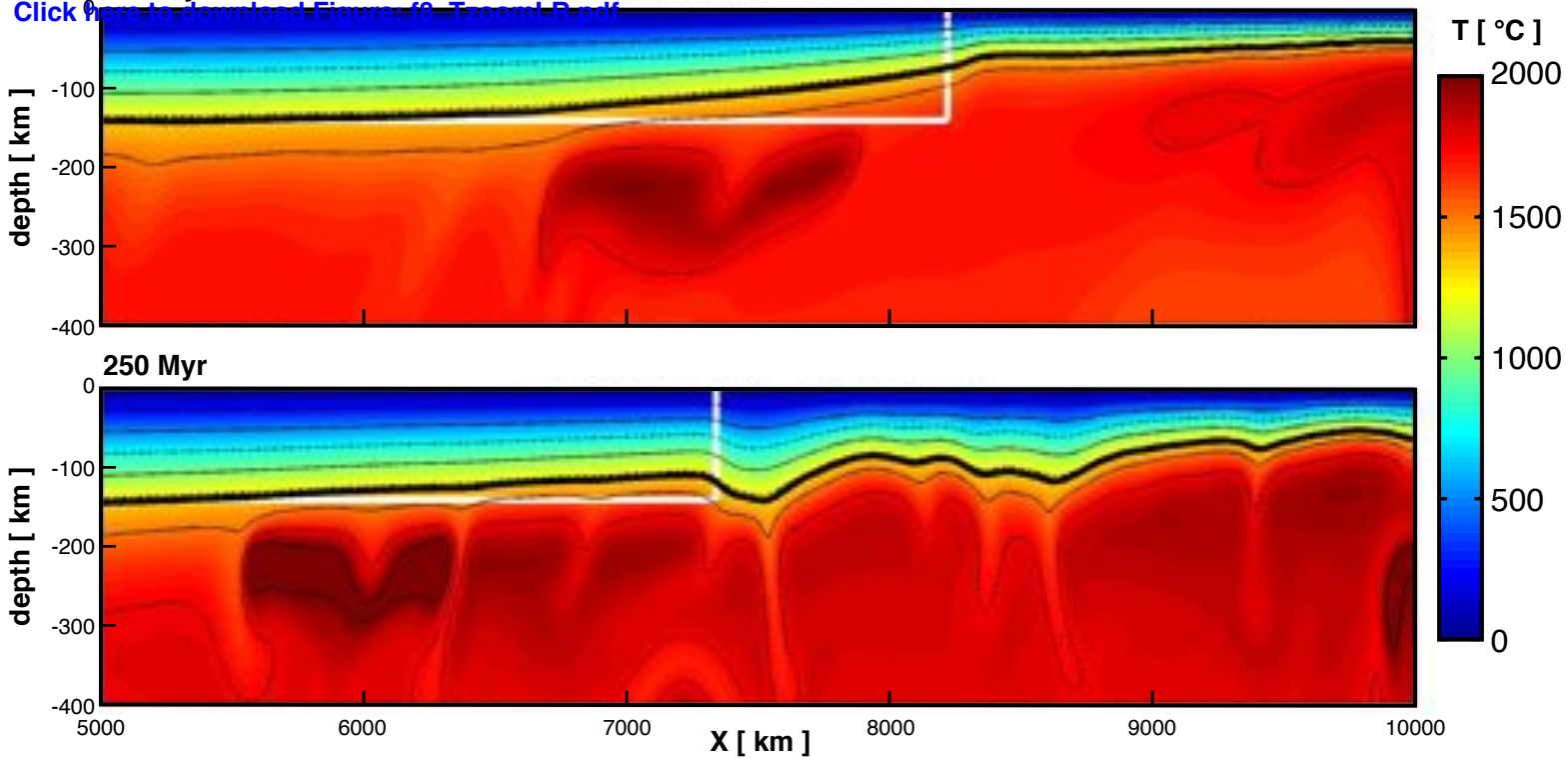


Figure 9

[Click here to download Figure: f9_TzftzTft3.pdf](#)

